

¹ A novel inf–sup–based volumetric constraint ratio and
² its implementation via mixed FE-meshfree formulation

³ Junchao Wu^{a,*}, Yingjie Chu^b, Yangtao Xu^a

^a Key Laboratory for Intelligent Infrastructure and Monitoring of Fujian Province, College
of Civil Engineering, Huaqiao University , Xiamen, Fujian, 361021, China

^b Fujian Key Laboratory of Digital Simulations for Coastal Civil Engineering, Department
of Civil Engineering, Xiamen University , Xiamen, Fujian, 361005, China

⁴ **Abstract**

Numerical formulations for incompressible materials often suffer from volumetric locking, which reduces the accuracy of displacement solutions and introduces oscillations in the pressure field. A well-chosen constraint ratio can mitigate this issue, but traditional approaches lack a theoretical foundation based on the inf–sup (or LBB) condition, which is essential for the stability of mixed formulations. This paper introduces a novel optimal constraint ratio derived from the inf–sup condition to address volumetric locking. The inf–sup test, a numerical tool for verifying the inf–sup condition, is reaffirmed to be equivalent to the inf–sup condition through a variational approach. By incorporating a complete polynomial space whose dimension matches the number of displacement degrees of freedom (DOFs), a new inf–sup value estimator is developed, explicitly considering the constraint ratio. For a given number of displacement DOFs, when the pressure DOFs of a numerical formulation remain below a stabilized number that falls into the optimal constraint ratio range, this numerical formulation actually satisfies the inf–sup condition. To implement the optimal constraint ratio, a mixed finite element and meshfree formulation is proposed, where displacements are discretized using traditional finite element approximations, and pressures are approximated via the reproducing kernel meshfree method. Leveraging the globally smooth reproducing kernel shape functions, the constraint ratio can be flexibly adjusted to meet the inf–sup condition without the limit of element. For computational efficiency and ease of implementation, pressure nodes are placed on selected displacement nodes to maintain the optimal constraint ratio. Inf–sup tests and a series of 2D and 3D incompressible elasticity examples validate the proposed constraint ratio, demonstrating its effectiveness in eliminating volumetric locking and enhancing the performance of mixed finite element and meshfree formulations.

⁵ **Keywords:** Optimal constraint ratio, Inf–sup condition estimator, Volumetric
⁶ locking, Mixed formulation, Reproducing kernel meshfree approximation

*Corresponding author

Email address: jcwu@hqu.edu.cn (Junchao Wu)

7 **1. Introduction**

8 The volumetric constraint is a necessary condition in the numerical formulation
 9 of incompressible materials like rubber and hydrogel. Proper imposition of
 10 this constraint is crucial for obtaining better numerical solutions; insufficient or
 11 excessive constraints will reduce the accuracy and stability of the solution [1].
 12 The volumetric constraint ratio [2], denoted as r , is often used to measure the
 13 level of constraint. It is defined as the total degrees of freedom (DOFs) of dis-
 14 placement divided by the total DOFs of pressure. Ideally, the optimal constraint
 15 ratio should be consistent with its governing partial differential equations. For
 16 example, in the two-dimensional (2D) case, the optimal constraint ratio is 2,
 17 since there are two governing equations for displacement and one for pressure.
 18 When the constraint ratio is less than 2, the formulation suffers from volumetric
 19 locking, while a constraint ratio greater than 2 can cause a coarse solution for
 20 pressure. These observations have been summarized as follows[2]:

$$r = \frac{2n_u}{n_p}, \quad \begin{cases} r > 2 & \text{too few constraints} \\ r = 2 & \text{optimal} \\ r < 2 & \text{too many constraints} \\ r \leq 1 & \text{severe locking} \end{cases} \quad (1)$$

21 where n_u and n_p are the numbers of control nodes for displacement and pressure,
 22 respectively. Classifying the locked status via the constraint ratio is straight-
 23 forward but imprecise. For instance, the constraint ratio can remain 2 while
 24 the pressure is discretized using continuous shape functions identical to the
 25 displacement's approximation. However, volumetric locking still exists in this
 26 formulation [2].

27 The inf-sup condition, also known as the Ladyzhenskay–Babuka–Brezzi
 28 (LBB) condition [3, 4], is a more precise requirement for a locking-free for-
 29 mulation. This condition is based on the mixed formulation framework, and
 30 when the inf-sup condition is satisfied, both the accuracy and stability of the
 31 mixed-formulation can be ensured. However, verifying the inf-sup condition is
 32 non-trivial. An eigenvalue problem namely inf-sup test can be used to check
 33 this condition numerically [5, 6, 7, 8]. Analytically, Brezzi and Fortin proposed
 34 a two-level projection framework that always satisfies the inf-sup condition, al-
 35 lowing it to be checked by identifying whether the formulation is included in
 36 this framework. Both analytical and numerical methods to check the inf-sup
 37 condition are complex, and the relationship between the constraint ratio and
 38 the inf-sup condition remains unclear.

39 To address volumetric constraint issues, adjusting the constraint ratio to an
 40 appropriate level is commonly used and easily implemented. In traditional finite
 41 element methods (FEM), this adjustment is carried out based on elements since
 42 the DOFs are embedded in each element. Conventional FEM often exhibits
 43 an over-constrained status. Reducing the approximation order of pressure in
 44 mixed formulation can alleviate the constraint burden, such as with the well-
 45 known Q4P1 (4-node quadrilateral displacement element with 1-node piecewise

constant pressure element) and Q8P3. Globally, using continuous shape functions to link the local pressure DOFs in each element can also reduce the total number of pressure DOFs and increase the constraint ratio, such as with T6C3 (6-node triangular displacement element with 3-node continuous linear pressure element) and Q9C4 (Taylor–Hood element) [9]. These schemes belong to the mixed formulation framework and can also be implemented through a projection approach, where the pressure approximant is projected into a lower-dimensional space. Examples include selective integration methods [10, 11], B–bar or F–bar methods [12, 13, 14, 15], pressure projection methods [16, 17, 18, 19, 20], and enhanced strain method [21]. Meanwhile, conventional 3-node triangular elements arranged in a regular cross pattern can also reduce the dimension of the pressure space [22]. It should be noted that not all of these methods meet the inf–sup condition despite alleviating volumetric locking and producing a good displacement solution. Some methods, like Q4P1, show significant oscillation for the pressure solution, known as spurious pressure mode or checkerboard mode [22]. In such cases, additional stabilization approaches, such as variational multi-scale stabilization (VMS) [23, 24, 25, 26, 27], Galerkin/least-squares (GLS) [28], or Streamline upwind/Petrov–Galerkin formulation (SUPG) [29, 30] are required to eliminate the oscillations in pressure.

Another class of FEM methods adjusts the constraint ratio by increasing the displacement DOFs. For instance, based on 3-node triangular elements, Arnold et al. [31, 32] used a cubic bubble function in each element to increase the displacement DOFs, known as the MINI element. It has been shown that this method belongs to the VMS framework [33], and its fulfillment of the inf–sup condition can be analytically evidenced using the two-level projection framework [7]. The Crouzeix–Raviart element [34] transfers the DOFs from the triangular vertices to edges, increasing the constraint ratio since, for triangular topology, the number of edges is greater than that of vertices. More details about FEM technology for volumetric constraint issues can be found in Refs. [2, 4, 35].

In the past two decades, various novel approximations equipped with globally smooth shape functions, such as moving least-squares approximation [36], reproducing kernel approximation [37, 38], radial basis functions [39, 40], maximum-entropy approximation [41], and NURBS approximation [42, 43], have been proposed. In these approaches, the approximant pressure evaluated by the derivatives of globally continuous shape functions also maintains a constraint ratio of 2 in 2D incompressible elasticity problems. However, the corresponding results still show lower accuracy caused by locking [44, 45]. Widely-used locking-free technologies for FEM are introduced in these approaches to enhance their performance. For example, Moutsanidis et al. [46, 47] employed selective integration and B–bar, F–bar methods for reproducing kernel particle methods. Wang et al. [48] applied selective integration schemes with bubble-stabilized functions to node-based smoothed particle FEM. Elguedj et al. [49] proposed the B–bar and F–bar NURBS formulations for linear and nonlinear incompressible elasticity. Chen et al. [50] adopted the pressure projection approach for reproducing kernel formulations for nearly-incompressible problems, which was later extended

to Stokes flow formulations by Goh et al. [51]. Bombarde et al. [52] developed a block-wise NURBS formulation for shell structures, eliminating locking via pressure projection. Casquero and Golestanian [53] proposed a NURBS-based continuous-assumed-strain element to alleviate volumetric locking. Most of these approximations offer better flexibility for arranging DOFs since their shape function constructions are no longer element-dependent. Huerta et al.[54] proposed a reproducing kernel approximation with divergence-free basis functions to avoid volumetric strain entirely , although this approach is unsuitable for compressible cases. Wu et al. [55] added extra displacement DOFs in FEM elements to resolve the locking issue, constructing local shape functions using generalized meshfree interpolation to maintain consistency. Vu-Huu et al. [56] employed different-order polygonal finite element shape functions to approximate displacement and pressure, embedding a bubble function in each element for stabilization.

This work proposes a more precise optimal volumetric constraint ratio and implements a locking-free mixed FE-meshfree formulation with this optimal constraint ratio. Firstly, the inf-sup condition is derived in a new form, showing that the inf-sup value equals to the lowest non-zero eigenvalue of dilatation stiffness in the context of variational analysis. Subsequently, involving a complete polynomial space with dimensions identical to displacement DOFs, the number of non-zero eigenvalues can be analytically calculated, and a new estimator considering the constraint ratio is established. From this estimator, the optimal constraint ratio is defined with a stabilized number of pressure nodes. If the constraint ratio exceeds the locking ratio, the formulation will show severe locking. When the constraint ratio is lower than the optimal ratio, the formulation achieves satisfactory results, and the inf-sup condition is fulfilled. This estimator provides a strong link between the inf-sup value and the pressure DOFs, making it possible to justify the locking status by counting the pressure nodes. Furthermore, a mixed FE-meshfree formulation is proposed to verify the optimal constraint ratio. In this mixed formulation, the displacement is approximated by traditional finite element methods, and the pressure is discretized by reproducing kernel meshfree approximation. With the aid of global RK shape functions, the pressure's DOFs can be adjusted arbitrarily without considering approximation order and numerical integration issues to maintaining the constraint ratio as optimal.

The remainder of this paper is organized as follows: Section 2 reviews the mixed formulation framework for incompressible elasticity problems. In Section 3, a novel estimator of the inf-sup value is developed, from which the optimal constraint ratio is obtained. Section 4 introduces the mixed FE-meshfree formulation and its corresponding nodal distribution schemes. Section 5 verifies the proposed optimal constraint ratio using a set of benchmark incompressible elasticity examples, studying error convergence and stability property for the mixed FE-meshfree approximation. Finally, the conclusions are presented in Section 6.

¹³⁶ **2. Mixed-formulation**

¹³⁷ *2.1. Nearly-incompressible elasticity*

¹³⁸ Consider a body $\Omega \in \mathbb{R}^{n_d}$ with boundary Γ in n_d -dimension, where Γ_t and
¹³⁹ Γ_g denote its natural boundary and essential boundary, respectively, such that
¹⁴⁰ $\Gamma_t \cup \Gamma_g = \Gamma$, $\Gamma_t \cap \Gamma_g = \emptyset$. The corresponding governing equations for the mixed
¹⁴¹ formulation are given by:

$$\begin{cases} \nabla \cdot \boldsymbol{\sigma} + \mathbf{b} = \mathbf{0} & \text{in } \Omega \\ \frac{p}{\kappa} + \nabla \cdot \mathbf{u} = 0 & \text{in } \Omega \\ \boldsymbol{\sigma} \cdot \mathbf{n} = \mathbf{t} & \text{on } \Gamma_t \\ \mathbf{u} = \mathbf{g} & \text{on } \Gamma_g \end{cases} \quad (2)$$

¹⁴² where \mathbf{b} denotes the prescribed body force in Ω . \mathbf{t}, \mathbf{g} are prescribed traction and
¹⁴³ displacement on natural and essential boundaries, respectively. \mathbf{u} and p , standing
¹⁴⁴ for displacement and hydrostatic pressure, respectively, are the variables of
¹⁴⁵ this problem. ∇ is the gradient tensor defined by $\nabla = \frac{\partial}{\partial x_i} \mathbf{e}_i$. $\boldsymbol{\sigma}$ denotes the
¹⁴⁶ stress tensor and has the following form:

$$\boldsymbol{\sigma}(\mathbf{u}, p) = p \mathbf{1} + 2\mu \nabla^d \mathbf{u} \quad (3)$$

¹⁴⁷ in which $\mathbf{1} = \delta_{ij} \mathbf{e}_i \otimes \mathbf{e}_j$ is the second-order identity tensor. $\nabla^d \mathbf{u}$ is the deviatoric
¹⁴⁸ gradient of \mathbf{u} and can be evaluated by:

$$\nabla^d \mathbf{u} = \frac{1}{2} (\mathbf{u} \nabla + \nabla \mathbf{u}) - \left(\frac{1}{3} \nabla \cdot \mathbf{u} \right) \mathbf{1} \quad (4)$$

¹⁴⁹ and κ, μ are the bulk modulus and shear modulus, respectively, and they can
¹⁵⁰ be represented by Young's modulus E and Poisson's ratio ν :

$$\kappa = \frac{E}{2(1-2\nu)}, \quad \mu = \frac{E}{3(1+\nu)} \quad (5)$$

¹⁵¹ In accordance with the Galerkin formulation, the weak form can be given
¹⁵² by: Find $\mathbf{u} \in V, p \in Q$, such that

$$\begin{cases} a(\mathbf{v}, \mathbf{u}) + b(\mathbf{v}, p) = f(\mathbf{v}) & \forall \mathbf{v} \in V \\ b(\mathbf{u}, q) + c(q, p) = 0 & \forall q \in Q \end{cases} \quad (6)$$

¹⁵³ with the spaces V, Q defined by:

$$V = \{\mathbf{v} \in H^1(\Omega)^2 \mid \mathbf{v} = \mathbf{g}, \text{ on } \Gamma_g\} \quad (7)$$

$$Q = \{q \in L^2(\Omega) \mid \int_{\Omega} q d\Omega = 0\} \quad (8)$$

¹⁵⁴ where $a : V \times V \rightarrow \mathbb{R}$, $b : V \times Q \rightarrow \mathbb{R}$ and $c : Q \times Q \rightarrow \mathbb{R}$ are bilinear forms,
¹⁵⁵ and $f : V \rightarrow \mathbb{R}$ is the linear form. In elasticity problems, they are given by:

$$a(\mathbf{v}, \mathbf{u}) = \int_{\Omega} \nabla^d \mathbf{v} : \nabla^d \mathbf{u} d\Omega \quad (9)$$

$$b(\mathbf{v}, q) = \int_{\Omega} \nabla \cdot \mathbf{v} q d\Omega \quad (10)$$

$$c(q, p) = - \int_{\Omega} \frac{1}{3\kappa} q p d\Omega \quad (11)$$

$$f(\mathbf{v}) = \int_{\Gamma_t} \mathbf{v} \cdot \mathbf{t} d\Gamma + \int_{\Omega} \mathbf{v} \cdot \mathbf{b} d\Omega \quad (12)$$

¹⁵⁶ 2.2. Ritz–Galerkin problem and volumetric locking

¹⁵⁷ In the mixed-formulation framework, the displacement and pressure can be
¹⁵⁸ discretized by different approximations. The approximant displacement \mathbf{u}_h and
¹⁵⁹ approximant pressure p_h can be expressed by:

$$\mathbf{u}_h(\mathbf{x}) = \sum_{I=1}^{n_u} N_I(\mathbf{x}) \mathbf{u}_I, \quad p_h(\mathbf{x}) = \sum_{K=1}^{n_p} \Psi_K(\mathbf{x}) p_K \quad (13)$$

¹⁶⁰ where N_I and Ψ_K are the shape functions for the displacement and pressure, \mathbf{u}_I
¹⁶¹ and p_K are the corresponding coefficients. Leading these approximations into
¹⁶² the weak form of Eq. (6) yields the following Ritz–Galerkin problems: Find
¹⁶³ $\mathbf{u}_h \in V_h$, $p_h \in Q_h$, such that

$$\begin{cases} a(\mathbf{v}_h, \mathbf{u}_h) + b(\mathbf{v}_h, p_h) = f(\mathbf{v}_h) & \forall \mathbf{v}_h \in V_h \\ b(\mathbf{u}_h, q_h) + c(q_h, p_h) = 0 & \forall q_h \in Q_h \end{cases} \quad (14)$$

¹⁶⁴ where the spaces $V_h \subseteq V$, $Q_h \subseteq Q$ are defined by:

$$V_h = \{\mathbf{v}_h \in (\text{span}\{N_I\}_{I=1}^{n_u})^{n_d} | \mathbf{v}_h = \mathbf{g}, \text{ on } \Gamma_g\} \quad (15)$$

$$Q_h = \{q_h \in \text{span}\{\Psi_K\}_{K=1}^{n_p} | \int_{\Omega} q_h d\Omega = 0\} \quad (16)$$

¹⁶⁵ For nearly incompressible material, the Poisson ratio approaches 0.5, and
¹⁶⁶ the bulk modulus κ will tend to infinity based on Eq. (5). Then, the bilinear
¹⁶⁷ form c in Eq. (11) tends to zero. And the weak form of Eq. (14) becomes an
¹⁶⁸ enforcement of the volumetric strain $\nabla \cdot \mathbf{u}_h$ to be zero using the Lagrangian
¹⁶⁹ multiplier method, where p_h is the Lagrangian multiplier.

¹⁷⁰ Furthermore, from the second line of Eq. (14), we have:

$$b(\mathbf{u}_h, q_h) + c(q_h, p_h) = (q_h, \nabla \cdot \mathbf{u}_h) - (q_h, \frac{1}{3\kappa} p_h) = 0, \quad \forall q_h \in Q_h \quad (17)$$

¹⁷¹ or

$$(q_h, 3\kappa \nabla \cdot \mathbf{u}_h - p_h) = 0, \quad \forall q_h \in Q_h \quad (18)$$

¹⁷² where (\bullet, \bullet) is the inner product operator evaluated by:

$$(q, p) := \int_{\Omega} q p d\Omega \quad (19)$$

¹⁷³ Obviously, in Eq. (18), p_h is the orthogonal projection of $3\kappa \nabla \cdot \mathbf{u}_h$ with respect
¹⁷⁴ to the space Q_h [1], and, for further development, we use the nabla notation
¹⁷⁵ with an upper tilde to denote the projection operator, i.e., $p_h = \tilde{\nabla} \cdot \mathbf{u}_h$. In this
¹⁷⁶ circumstance, the bilinear form b in the first line of Eq. (14) becomes:

$$\begin{aligned} b(\mathbf{v}_h, p_h) &= (\underbrace{\nabla \cdot \mathbf{v}_h - \tilde{\nabla} \cdot \mathbf{v}_h, p_h}_{0}) + (\tilde{\nabla} \cdot \mathbf{v}_h, \underbrace{p_h}_{3\kappa \tilde{\nabla} \cdot \mathbf{u}_h}) \\ &= (\tilde{\nabla} \cdot \mathbf{v}_h, 3\kappa \tilde{\nabla} \cdot \mathbf{u}_h) \\ &= \tilde{a}(\mathbf{v}_h, \mathbf{u}_h) \end{aligned} \quad (20)$$

¹⁷⁷ where the bilinear form $\tilde{a} : V_h \times V_h \rightarrow \mathbb{R}$ is defined by:

$$\tilde{a}(\mathbf{v}_h, \mathbf{u}_h) = \int_{\Omega} 3\kappa \tilde{\nabla} \cdot \mathbf{v}_h \tilde{\nabla} \cdot \mathbf{u}_h d\Omega \quad (21)$$

¹⁷⁸ Accordingly, the problem of Eq. (14) becomes a one-variable form: Find
¹⁷⁹ $\mathbf{u}_h \in V_h$, such that

$$a(\mathbf{v}_h, \mathbf{u}_h) + \tilde{a}(\mathbf{v}_h, \mathbf{u}_h) = f(\mathbf{v}_h), \quad \forall \mathbf{v}_h \in V_h \quad (22)$$

¹⁸⁰ As $\kappa \rightarrow \infty$, Eq. (22) can be regarded as an enforcement of volumetric strain
¹⁸¹ using the penalty method, where \tilde{a} is the penalty term. However, it should
¹⁸² be noted that, if the mixed-formulation wants to obtain a satisfactory result,
¹⁸³ this orthogonal projection must be surjective [57]. In the case where it is not
¹⁸⁴ surjective, for a given $p_h \in Q_h$, it may not be possible to find a $\mathbf{u}_h \in V_h$ such that
¹⁸⁵ $p_h = 3\kappa \nabla \cdot \mathbf{u}_h$. This will lead to a much smaller displacement than expected and
¹⁸⁶ an oscillated pressure result. This phenomenon is called volumetric locking.

¹⁸⁷ 3. Optimal volumetric constraint ratio

¹⁸⁸ 3.1. Inf-sup condition and its eigenvalue problem

¹⁸⁹ To ensure the surjectivity of orthogonal projection and satisfactory results,
¹⁹⁰ the approximations of Eq.(7) should satisfy the inf-sup condition, also known
¹⁹¹ as the Ladyzhenskaya–Babuška–Brezzi condition [4]:

$$\inf_{q_h \in Q_h} \sup_{\mathbf{v}_h \in V_h} \frac{|b(q_h, \mathbf{v}_h)|}{\|q_h\|_Q \|\mathbf{v}_h\|_V} \geq \beta > 0 \quad (23)$$

¹⁹² in which β , namely the inf-sup value, is a constant independent of the charac-
¹⁹³ terized element size h . The norms $\|\bullet\|_V$ and $\|\bullet\|_Q$ can be flexibly defined

¹⁹⁴ by:

$$\|\mathbf{v}\|_V^2 := \int_{\Omega} \nabla^d \mathbf{v} : \nabla^d \mathbf{v} d\Omega \quad (24)$$

$$\|q\|_Q^2 := \int_{\Omega} \frac{1}{3\kappa} q^2 d\Omega \quad (25)$$

¹⁹⁵ Additionally, the Appendix A lists the displacement and pressure error estimators for the mixed-formulations. This indicates how the inf-sup value β affects ¹⁹⁶ the solution accuracy.

¹⁹⁸ To establish the relationship between the inf-sup condition and the constraint ratio, the inf-sup condition is firstly transformed by the following Lemma ¹⁹⁹ 1:

²⁰¹ **Lemma 1.** Suppose $\mathcal{P}_h : V_h \rightarrow Q_h$ is the orthogonal projection operator of the ²⁰² divergence operator $\mathcal{P} := 3\kappa \nabla \cdot$, i.e., $\mathcal{P}_h := 3\kappa \tilde{\nabla} \cdot$ and satisfies Eq. (18). Then, ²⁰³ the inf-sup value can be estimated by:

$$\beta \leq \inf_{V'_h \subset V_h \setminus \ker \mathcal{P}_h} \sup_{\mathbf{v}_h \in V'_h} \frac{\|\mathcal{P}_h \mathbf{v}_h\|_Q}{\|\mathbf{v}_h\|_V} \quad (26)$$

²⁰⁴ in which $\ker \mathcal{P}_h \subset V_h$ is the kernel of \mathcal{P}_h defined by $\ker \mathcal{P}_h := \{\mathbf{v}_h \in V_h \mid \mathcal{P}_h \mathbf{v}_h = 0\}$.

²⁰⁶ PROOF. First, define the image space of \mathcal{P}_h as $\text{Im} \mathcal{P}_h := \{p_h \in Q_h \mid \exists \mathbf{v}_h \in V_h, p_h = \mathcal{P}_h \mathbf{v}_h\}$. Since $\mathcal{P}_h \subset Q_h$, Eq. (23) can be rewritten as:

$$\begin{aligned} \beta &\leq \inf_{q_h \in Q_h} \sup_{\mathbf{v}_h \in V_h} \frac{|b(q_h, \mathbf{v}_h)|}{\|q_h\|_Q \|\mathbf{v}_h\|_V} = \inf_{q_h \in Q_h} \sup_{\mathbf{v}_h \in V_h} \frac{|(q_h, \frac{1}{3\kappa} \mathcal{P} \mathbf{v}_h)|}{\|q_h\|_Q \|\mathbf{v}_h\|_V} \\ &\leq \inf_{q_h \in \text{Im} \mathcal{P}_h} \sup_{\mathbf{v}_h \in V_h} \frac{|\frac{1}{3\kappa} (q_h, \mathcal{P}_h \mathbf{v}_h)|}{\|q_h\|_Q \|\mathbf{v}_h\|_V} \end{aligned} \quad (27)$$

²⁰⁸ For a given $q_h \in \text{Im} \mathcal{P}_h$, since both q_h and $\mathcal{P}_h \mathbf{v}_h$ belong to $\text{Im} \mathcal{P}_h$, $\text{Im} \mathcal{P}_h \subset Q_h$, ²⁰⁹ according to the Cauchy-Schwarz inequality, we have:

$$\left| \frac{1}{3\kappa} (q_h, \mathcal{P}_h \mathbf{v}_h) \right| \leq \|q_h\|_Q \|\mathcal{P}_h \mathbf{v}_h\|_Q \quad (28)$$

²¹⁰ where this equality holds if and only if $q_h = \mathcal{P}_h \mathbf{v}_h$, i.e.,

$$\left| \frac{1}{3\kappa} (q_h, \mathcal{P}_h \mathbf{v}_h) \right| = \|q_h\|_Q \|\mathcal{P}_h \mathbf{v}_h\|_Q, \quad \forall \mathbf{v}_h \in V'_h \quad (29)$$

²¹¹ the space $V'_h \subseteq V_h \setminus \ker \mathcal{P}_h$ defined by:

$$V'_h = \{\mathbf{v}_h \in V_h \mid \mathcal{P}_h \mathbf{v}_h = q_h\} \quad (30)$$

²¹² And the following relationship can be evidenced:

$$\sup_{\mathbf{v}_h \in V_h} \frac{|\frac{1}{3\kappa} (q_h, \mathcal{P}_h \mathbf{v}_h)|}{\|q_h\|_Q \|\mathbf{v}_h\|_V} = \sup_{\mathbf{v}_h \in V'_h} \frac{\|\mathcal{P}_h \mathbf{v}_h\|_Q}{\|\mathbf{v}_h\|_V}, \quad \exists q_h \in \text{Im} \mathcal{P}_h \quad (31)$$

²¹³ Consequently, by combining Eqs. (27) and (31), Eq. (26) can be obtained.

²¹⁴ **Remark 1.** With Lemma 1 and the norm definitions in Eqs. (24),(25), the
²¹⁵ square of the inf-sup value can further be bounded by:

$$\beta^2 \leq \inf_{V'_h \subset V_h \setminus \ker \mathcal{P}_h} \sup_{\mathbf{v}_h \in V'_h} \frac{\|\mathcal{P}_h \mathbf{v}_h\|_Q^2}{\|\mathbf{v}_h\|_V^2} = \inf_{V'_h \subset V_h \setminus \ker \mathcal{P}_h} \sup_{\mathbf{v}_h \in V'_h} \frac{\tilde{a}(\mathbf{v}_h, \mathbf{v}_h)}{a(\mathbf{v}_h, \mathbf{v}_h)} \quad (32)$$

²¹⁶ The left-hand side of the above equation is consistent with the minimum-maximum
²¹⁷ principle [58] and again proves the equivalence with the traditional numerical
²¹⁸ inf-sup test [5]. Since that, β^2 evaluates the non-zero general eigenvalue of \tilde{a}
²¹⁹ and a in Eq. (22).

²²⁰ 3.2. Inf-sup value estimator

²²¹ Subsequently, the relationship between constraint ratio and the inf-sup con-
²²² dition is established by the following Theorem:

²²³ **Theorem 1.** Suppose that P_{n_u} is a complete polynomial space with n_u dimen-
²²⁴ sions, and V_{n_u} is the polynomial displacement space, $V_{n_u} = P_{n_u}^{n_d}$. The inf-sup
²²⁵ value β can further be bounded by:

$$\beta \leq \beta_s + O(h) \quad (33)$$

²²⁶ with

$$\beta_s = \inf_{V' \subset V_{n_u} \setminus \ker \mathcal{P}_h \mathcal{I}_h} \sup_{\mathbf{v} \in V'} \frac{\|\mathcal{P} \mathbf{v}\|_Q}{\|\mathbf{v}\|_V} \quad (34)$$

²²⁷ where \mathcal{I}_h is the interpolation operator of the displacement approximation, and
²²⁸ correspondingly, $O(h)$ is the remainder related to h .

²²⁹ PROOF. As the dimensions of V_h and V_{n_u} are identical, $\dim V_{n_u} = \dim V_h =$
²³⁰ $n_d \times n_u$. There exists a unique $\mathbf{v} \in V_{n_u}$ satisfying $\mathbf{v}_h = \mathcal{I}_h \mathbf{v}$. And the right side
²³¹ of Eq. (26) becomes:

$$\inf_{V'_h \subset V_h \setminus \ker \mathcal{P}_h} \sup_{\mathbf{v}_h \in V'_h} \frac{\|\mathcal{P}_h \mathbf{v}_h\|_Q}{\|\mathbf{v}_h\|_V} = \inf_{V' \subset V_{n_u} \setminus \ker \mathcal{P}_h \mathcal{I}_h} \sup_{\mathbf{v} \in V'} \frac{\|\mathcal{P}_h \mathcal{I}_h \mathbf{v}\|_Q}{\|\mathcal{I}_h \mathbf{v}\|_V} \quad (35)$$

²³² According to the triangular inequality, Cauchy-Schwarz inequality, and the
²³³ relationship of Eqs. (18), we have:

$$\begin{aligned} \|\mathcal{P}_h \mathcal{I}_h \mathbf{v}\|_Q &= \sup_{q_h \in Q_h} \frac{|\frac{1}{3\kappa}(q_h, \mathcal{P}_h \mathcal{I}_h \mathbf{v})|}{\|q_h\|_Q} = \sup_{q_h \in Q_h} \frac{|\frac{1}{3\kappa}(q_h, \mathcal{P} \mathcal{I}_h \mathbf{v})|}{\|q_h\|_Q} \\ &\leq \sup_{q_h \in Q_h} \frac{|\frac{1}{3\kappa}(q_h, \mathcal{P} \mathbf{v})| + |\frac{1}{3\kappa}(q_h, \mathcal{P} \mathbf{v} - \mathcal{P} \mathcal{I}_h \mathbf{v})|}{\|q_h\|_Q} \\ &\leq \|\mathcal{P} \mathbf{v}\|_Q + \|\mathcal{P}(\mathbf{v} - \mathcal{I}_h \mathbf{v})\|_Q \end{aligned} \quad (36)$$

²³⁴ Obviously, the second term on the right side of Eq. (36) is the interpolation
²³⁵ error, and can be evaluated by [59]:

$$\|\mathcal{P}(\mathbf{v} - \mathcal{I}_h \mathbf{v})\|_Q \leq Ch^k |\mathbf{v}|_{H_k} \quad (37)$$

236 where, for a sufficiently smooth $\mathbf{v} \in V$, k equals to the interpolation order of
 237 \mathcal{I}_h .

238 Further leading the relation $\|\mathcal{I}_h \mathbf{v}\|_V \geq C|\mathbf{v}|_{H_k}$ obtained from the closed
 239 graph theorem [33] and considering Eqs. (36)-(37), the right-hand side of Eq.
 240 (35) can be represented as:

$$\inf_{V' \subset V_{n_u} \setminus \ker \mathcal{P}_h \mathcal{I}_h} \sup_{\mathbf{v} \in V'} \frac{\|\mathcal{P}_h \mathcal{I}_h \mathbf{v}\|_Q}{\|\mathcal{I}_h \mathbf{v}\|_V} \leq \inf_{V' \subset V_{n_u} \setminus \ker \mathcal{P}_h \mathcal{I}_h} \sup_{\mathbf{v} \in V'} \frac{\|\mathcal{P} \mathbf{v}\|_Q}{\|\mathbf{v}\|_V} + O(h) \quad (38)$$

241 Substituting Eqs. (35),(38) into (26) finally proves Eqs. (33), (34).

242 As we can see in Eqs. (33) and (34), $\beta_s \geq 0$, the condition that β_s being
 243 equal to 0 or not determines whether the formulation can satisfy the inf-sup
 244 condition. If $\beta_s > 0$, as the mesh refines, the second term on the right-hand
 245 side of Eq. (33) will sharply reduce and can be ignored. In contrast, if $\beta_s = 0$,
 246 the second term will dominate, and the evaluation of β will be dependent to h .
 247 Therefore, the inf-sup condition is violated and numerical instability arises.

248 3.3. Polynomial-wise constraint counting

249 From the above subsection, we can know that whether β_s is zero or not
 250 determines whether the mixed-formulation can fulfill the inf-sup condition. Ac-
 251 cording to the expression of β_s in Eq. (34), as $\beta_s = 0$, the variable \mathbf{v} should
 252 belong to $\ker \mathcal{P}$, so the dimensions of the subspace in which $\beta_s \neq 0$, namely n_s ,
 253 can be evaluated by:

$$n_s = \dim(V_{n_u} \setminus \ker \mathcal{P}) \quad (39)$$

254 To further construct the relationship between the inf-sup value estimator in
 255 Eq. (33) and the constraint ratio $r = \frac{n_d \times n_u}{n_p}$, we should find the displacement
 256 and pressure DOFs in Eq. (33). With the definition of V_{n_u} , the number of
 257 displacement DOFs is easy to be evaluated by:

$$n_d \times n_u = \dim V_{n_u} \quad (40)$$

258 With well-posed nodal distributions of displacement and pressure, the number
 259 of pressure DOFs has the following relationship:

$$n_p = \dim Q_h = \dim(\text{Im} \mathcal{P}_h) = \dim(V_{n_u} \setminus \ker \mathcal{P}_h \mathcal{I}_h) \quad (41)$$

260 Figure 1 illustrates how the relationship between n_s , n_p , and n_u influences
 261 the fulfillment of the inf-sup condition:

- 262 • As $n_p > n_s$, there must exist a subspace in space $V_{n_u} \setminus \ker \mathcal{P}_h \mathcal{I}_h$ belonging
 263 to $\ker \mathcal{P}$, resulting in $\beta_s = 0$, i.e., $V_{n_u} \setminus \ker \mathcal{P}_h \mathcal{I}_h \cap \ker \mathcal{P} \neq \emptyset$. At this cir-
 264 cumstance, the inf-sup condition cannot be satisfied, and the formulation
 265 will suffer from volumetric locking.
- 266 • As $n_p \leq n_s$, for well-posed nodal distributions, the space $V_{n_u} \setminus \ker \mathcal{P}_h \mathcal{I}_h$
 267 may be a subset of $V_{n_u} \setminus \ker \mathcal{P}$. Then, β_s will remain nonzero, and the
 268 formulation will be locking-free.

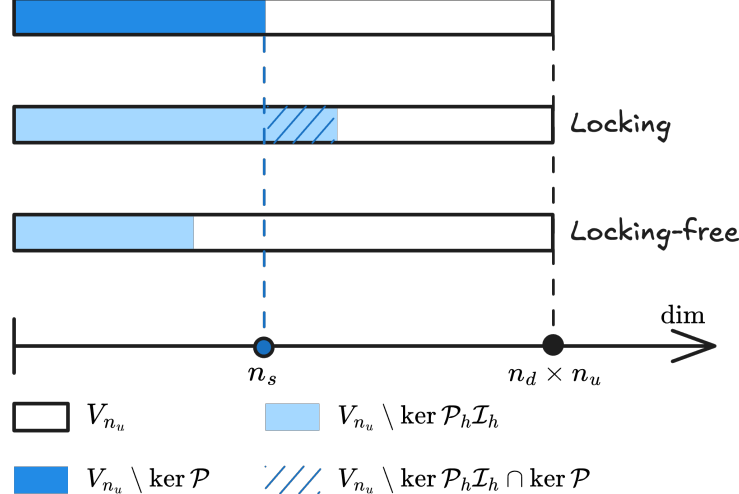


Figure 1: Illustration of estimator

269 Summarily, the formulation can satisfy the inf-sup condition and alleviate
 270 volumetric locking if at least the number of pressure nodes n_p is less than n_s ,
 271 so we name n_s as the stabilized number of pressure nodes. At this moment,
 272 the volumetric constraint ratio should meet the following relation to ensure the
 273 inf-sup condition:

$$r_{opt} \geq \frac{n_d \times n_u}{n_s} \quad (42)$$

274 **Remark 2.** *Some uniform elements with special arrangements, like the union-*
 275 *jack element arrangement for 3-node triangular elements, can pass the inf-sup*
 276 *test [6], but their pressure DOFs number is greater than n_s . This is because the*
 277 *union-jack arrangement leads to a lower nonzero eigenvalue number of $\tilde{\alpha}$ and a*
 278 *in Eq. (22), and the corresponding nonzero eigenvalue number is less than or*
 279 *equal to the stabilized number n_s , satisfying Eq. (42). The similar cases about*
 280 *this special element arrangement are too few, so it is more straightforward to*
 281 *use the number of pressure nodes n_p to measure $\dim(V_{n_u} \setminus \ker \mathcal{P}_{h\mathcal{I}_h})$.*

282 **Remark 3.** *It is obvious that the traditional optimal constraint ratio cannot*
 283 *fulfill this condition. However, not all formulations satisfying this condition can*
 284 *totally avoid volumetric locking. This is because $n_p \leq n_s$ is not equivalent to*
 285 *$V_{n_u} \setminus \ker \mathcal{P}_{h\mathcal{I}_h} \subset V_{n_u} \setminus \ker \mathcal{P}$. Fortunately, well-posed nodal distributions of*
 286 *displacement and pressure can ensure this, which will be evidenced by numerical*
 287 *examples in the subsequent sections.*

288 3.4. Optimal volumetric constraint ratio

289 The fulfillment of the inf-sup condition should require the number of pres-
 290 sure nodes n_p to be lower than the stabilized number n_s , and now, we will
 291 demonstrate how to determine n_s for a specific number of displacement DOFs.

²⁹² In the 2D case, for instance, we first consider the linear polynomial displace-
²⁹³ ment space V_3 that is given by:

$$V_3 = \text{span} \left\{ \begin{pmatrix} 1 \\ 0 \end{pmatrix}, \begin{pmatrix} 0 \\ 1 \end{pmatrix}, \begin{pmatrix} x \\ 0 \end{pmatrix}, \begin{pmatrix} 0 \\ x \end{pmatrix}, \begin{pmatrix} y \\ 0 \end{pmatrix}, \begin{pmatrix} 0 \\ y \end{pmatrix} \right\} \quad (43)$$

²⁹⁴ or rearranged as follows,

$$V_3 = \text{span} \left\{ \underbrace{\begin{pmatrix} 1 \\ 0 \end{pmatrix}, \begin{pmatrix} 0 \\ 1 \end{pmatrix}, \begin{pmatrix} y \\ 0 \end{pmatrix}, \begin{pmatrix} 0 \\ x \end{pmatrix}, \begin{pmatrix} x \\ -y \end{pmatrix}}_{\ker \mathcal{P}}, \underbrace{\begin{pmatrix} x \\ y \end{pmatrix}}_{V_3 \setminus \ker \mathcal{P}} \right\} \quad (44)$$

²⁹⁵ It can be counted that, for $n_u = 3$, $n_s = 1$. Following the path, the displacement
²⁹⁶ space with a quadratic polynomial base, namely V_6 , can be stated as:

$$V_6 = \text{span} \left\{ \underbrace{\begin{pmatrix} 1 \\ 0 \end{pmatrix}, \begin{pmatrix} 0 \\ 1 \end{pmatrix}, \begin{pmatrix} y \\ 0 \end{pmatrix}, \begin{pmatrix} 0 \\ x \end{pmatrix}, \begin{pmatrix} x \\ -y \end{pmatrix}, \begin{pmatrix} x^2 \\ -2xy \end{pmatrix}, \begin{pmatrix} y^2 \\ 0 \end{pmatrix}, \begin{pmatrix} 0 \\ x^2 \end{pmatrix}, \begin{pmatrix} -2xy \\ y^2 \end{pmatrix}}_{\ker \mathcal{P}}, \underbrace{\begin{pmatrix} x \\ y \end{pmatrix}, \begin{pmatrix} x^2 \\ 2xy \end{pmatrix}, \begin{pmatrix} 2xy \\ y^2 \end{pmatrix}}_{V_6 \setminus \ker \mathcal{P}} \right\} \quad (45)$$

²⁹⁷ In this circumstance, $n_s = 3$. As the order of the polynomial space increases,
²⁹⁸ the optimal numbers of constraint DOFs for each order of the polynomial space
²⁹⁹ are listed in Table. 1, in which n denotes the order of space P_{n_u} . For the
³⁰⁰ flexibility of usage, the relation between n_u and n_s is summarized as follows:

$$n_s = \frac{n(n+1)}{2}, \quad n = \left\lfloor \frac{\sqrt{1+8n_u}-3}{2} \right\rfloor \quad (46)$$

³⁰¹ where $\lfloor \bullet \rfloor$ denotes the floor function.

Table 1: Relationship between the number of displacement nodes n_u and stabilized number of pressure nodes n_s

n	2D		3D	
	n_u	n_s	n_u	n_s
1	3	1	4	1
2	6	3	10	4
3	10	6	20	10
4	15	10	35	20
\vdots	\vdots	\vdots	\vdots	\vdots

³⁰² For the 3D case, following the path in 2D, the linear polynomial space V_4 is

³⁰³ considered herein, and the arranged space of V_4 is listed as follows:

$$V_4 = \text{span} \left\{ \underbrace{\begin{pmatrix} 1 \\ 0 \\ 0 \\ 0 \end{pmatrix}, \begin{pmatrix} 0 \\ 1 \\ 0 \\ 0 \end{pmatrix}, \begin{pmatrix} 0 \\ 0 \\ 1 \\ 0 \end{pmatrix}, \begin{pmatrix} 0 \\ x \\ 0 \\ 0 \end{pmatrix}, \begin{pmatrix} 0 \\ 0 \\ x \\ 0 \end{pmatrix}, \begin{pmatrix} y \\ 0 \\ 0 \\ 0 \end{pmatrix}}_{\ker \mathcal{P}}, \underbrace{\begin{pmatrix} 0 \\ 0 \\ y \\ 0 \end{pmatrix}, \begin{pmatrix} z \\ 0 \\ 0 \\ 0 \end{pmatrix}, \begin{pmatrix} 0 \\ z \\ 0 \\ 0 \end{pmatrix}, \begin{pmatrix} x \\ -y \\ 0 \\ 0 \end{pmatrix}, \begin{pmatrix} x \\ 0 \\ -z \\ 0 \end{pmatrix}, \begin{pmatrix} x \\ y \\ z \\ 0 \end{pmatrix}}_{V_{n_u} \setminus \ker \mathcal{P}} \right\} \quad (47)$$

³⁰⁴ For brevity, the stabilized numbers for higher-order polynomial displacement
³⁰⁵ spaces are directly listed in Table. 1, and it can be summarized that, for a given
³⁰⁶ number of displacement DOFs, the stabilized number for pressure DOFs can be
³⁰⁷ calculated as follows:

$$n_s = \frac{n(n+1)(n+2)}{6} \quad (48)$$

$$n = \left[\left(3n_u + \frac{1}{3} \sqrt{81n_u^2 - \frac{1}{3}} \right)^{\frac{1}{3}} + \frac{1}{3 \left(3n_u + \frac{1}{3} \sqrt{81n_u^2 - \frac{1}{3}} \right)^{\frac{1}{3}}} - 2 \right] \quad (49)$$

³⁰⁸ 4. Mixed FE–meshfree formulation with optimal constraint ratio

³⁰⁹ In the proposed mixed–formulation, the displacement is approximated using
³¹⁰ 3-node (Tri3), 6-node (Tri6) triangular elements and 4-node (Quad4), 8-node
³¹¹ (Quad8) quadrilateral elements in 2D, 4-node (Tet4) tetrahedral element and
³¹² 8-node (Hex8) hexahedral element in 3D [2]. In order to flexibly adjust to let
³¹³ the DOFs of pressure meet the optimal constraint, the reproducing kernel (RK)
³¹⁴ meshfree approximation is involved to approximate pressure, namely “FE”–RK
³¹⁵ formulation.

³¹⁶ 4.1. Reproducing kernel meshfree approximation

³¹⁷ In accordance with the reproducing kernel approximation, the entire domain
³¹⁸ Ω , as shown in Figure 2, is discretized by n_p meshfree nodes, $\{\mathbf{x}_I\}_{I=1}^{n_p}$. The
³¹⁹ approximated pressure, namely p_h , can be expressed by the shape function Ψ_I
³²⁰ and nodal coefficient p_I , yields:

$$p_h(\mathbf{x}) = \sum_{I=1}^{n_p} \Psi_I(\mathbf{x}) p_I \quad (50)$$

³²¹ where, in the reproducing kernel approximation framework, the shape function
³²² Ψ_I is given by:

$$\Psi_I(\mathbf{x}) = \mathbf{c}(\mathbf{x}_I - \mathbf{x}) \mathbf{p}(\mathbf{x}_I - \mathbf{x}) \phi(\mathbf{x}_I - \mathbf{x}) \quad (51)$$

³²³ in which \mathbf{p} is the basis vector, for instance in the context of the 3D quadratic
³²⁴ case, the basis vector takes the following form:

$$\mathbf{p}(\mathbf{x}) = \{1, x, y, z, x^2, y^2, z^2, xy, xz, yz\}^T \quad (52)$$

³²⁵ and ϕ stands for the kernel function. In this work, the traditional Cubic B-spline
³²⁶ function with square or cube support is used as the kernel function:

$$\phi(\mathbf{x}_I - \mathbf{x}) = \phi(s_x)\phi(s_y)\phi(s_z), \quad s_i = \frac{\|\mathbf{x}_I - \mathbf{x}\|}{\bar{s}_{iI}} \quad (53)$$

³²⁷ with

$$\phi(s) = \frac{1}{3!} \begin{cases} (2-2s)^3 - 4(1-2s)^3 & s \leq \frac{1}{2} \\ (2-2s)^3 & \frac{1}{2} < s < 1 \\ 0 & s > 1 \end{cases} \quad (54)$$

³²⁸ where \bar{s}_{iI} 's are the support size towards the i -direction for the shape function
³²⁹ Ψ_I . The correction function \mathbf{c} can be determined by the following so-called
³³⁰ consistency condition:

$$\sum_{I=1}^{n_p} \Psi_I(\mathbf{x}) \mathbf{p}(\mathbf{x}_I) = \mathbf{p}(\mathbf{x}) \quad (55)$$

³³¹ or equivalent shifted form:

$$\sum_{I=1}^{n_p} \Psi_I(\mathbf{x}) \mathbf{p}(\mathbf{x}_I - \mathbf{x}) = \mathbf{p}(\mathbf{0}) \quad (56)$$

³³² The consistency condition ensures that the reproducing kernel shape functions
³³³ are able to reproduce the polynomial space spanned by the basis function \mathbf{p} ,
³³⁴ which is a fundamental requirement for the accuracy of the Galerkin method.
³³⁵ Herein, the order of the basis function \mathbf{p} is chosen to be the same as the order
³³⁶ of the displacement approximation.

³³⁷ Further, substituting Eq. 51 into Eq. (56) leads to:

$$\mathbf{c}(\mathbf{x}_I - \mathbf{x}) = \mathbf{A}^{-1}(\mathbf{x}_I - \mathbf{x}) \mathbf{p}(\mathbf{0}) \quad (57)$$

³³⁸ in which \mathbf{A} is namely the moment matrix evaluated by:

$$\mathbf{A}(\mathbf{x}_I - \mathbf{x}) = \sum_{I=1}^{n_p} \mathbf{p}(\mathbf{x}_I - \mathbf{x}) \mathbf{p}^T(\mathbf{x}_I - \mathbf{x}) \phi(\mathbf{x}_I - \mathbf{x}) \quad (58)$$

³³⁹ Taking Eq. (57) back to Eq. (51), the final form of the reproducing kernel shape
³⁴⁰ function can be obtained as:

$$\Psi_I(\mathbf{x}) = \mathbf{p}^T(\mathbf{0}) \mathbf{A}^{-1}(\mathbf{x}_I - \mathbf{x}) \phi(\mathbf{x}_I - \mathbf{x}) \quad (59)$$

³⁴¹ As shown in Figure 2, reproducing kernel meshfree shape functions are glob-
³⁴² ally smooth across the entire domain, using them to discretize the pressure field

343 allows the constraint ratio to be adjusted arbitrarily, without being limited by
 344 element topology. Meshfree shape functions generally lack the Kronecker delta
 345 property, which prevents the direct imposition of essential boundary conditions.
 346 Fortunately, the mixed formulation shown in Eq. 14 only concerns the displace-
 347 ment essential boundary condition, and this condition can be easily imposed by
 348 the standard methods, such as the penalty method that used in this work.

349 Moreover, when combined with finite element approximations in Eq. 14,
 350 numerical integration can be conveniently performed within each finite element
 351 (Ω_C 's). The numerical integration issue caused by the loss of variational con-
 352 sistency between meshfree shape functions and their derivatives [60] would not
 353 appear in the mixed formulation of Eq. 14, this is due to the fact that Eq.
 354 14 solely depends on the meshfree shape functions themselves. Therefore, the
 355 proposed method employs standard lower-order Gaussian quadrature rules, as
 356 commonly used in traditional finite element methods, while still maintaining its
 357 accuracy. Table 2 lists the integration schemes used in this work for mixed-
 358 formulations. Methods with linear basis functions use an integration scheme of
 359 order 2. Those with quadratic basis functions use a scheme of order 4. The
 360 detailed locations and weights of the Gauss points can be found in Ref. [4].

Table 2: Integration schemes for the mixed FE–meshfree formulation

Methods	n_o	n_g for Ω	n_g for Γ
Tri3-RK	2	3	2
Tri6-RK	4	6	3
Quad4-RK	2	2×2	2
Quad8-RK	4	3×3	3
Tet4-RK	2	4	3
Hex8-RK	2	$2 \times 2 \times 2$	4

n_o : Integration Order n_g : Number of integration points

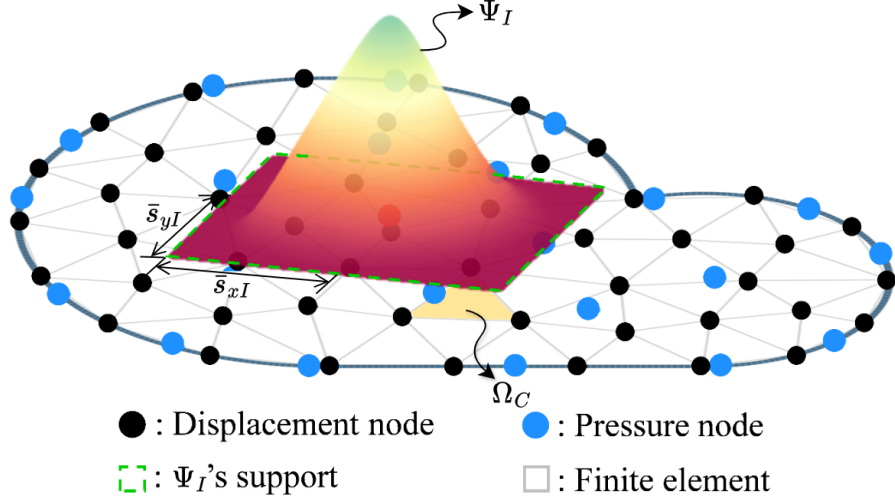


Figure 2: Illustration for reproducing kernel meshfree approximation

361 *4.2. Pressure node distributions with optimal constraint ratio*

362 In this subsection, 2D and 3D inf-sup tests [6], as defined in Eq. 32, are
363 conducted using the mixed FE-meshfree formulations to validate the proposed
364 inf-sup value estimator. The 2D test considers the square domain $\Omega = (0, 1) \times$
365 $(0, 1)$, where the displacement is discretized by Tri3 and Quad4 with 4×4 ,
366 8×8 , 16×16 and 32×32 elements, Tri6 and Quad8 with 2×2 , 4×4 , 8×8
367 and 16×16 elements, respectively. The 3D test employs a cube domain $\Omega =$
368 $(0, 1) \times (0, 1) \times (0, 1)$ with 4×4 , 8×8 and 16×16 elements for the Tet4 and Hex8.
369 For pressure discretization, linear meshfree approximation with a normalized
370 support size of 1.5 is employed for Tri3, Quad4, Tet4 and Hex8. For Tri6 and
371 Quad8, a quadratic meshfree approximation with a normalized support size of
372 2.5 is utilized. In order to avoid the influence of interpolation error, uniform
373 nodal distributions are used for pressure discretizations, for example in Figure
374 3, which displays 4×4 Quad4 elements with 4×3 uniformly distributed pressure
375 nodes.

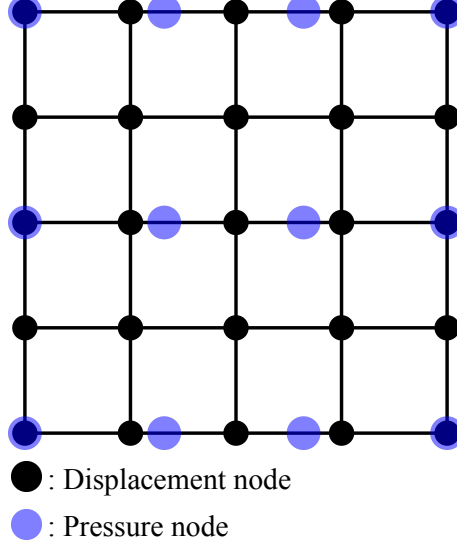


Figure 3: Illustration of uniform nodal distribution for inf-sup test with $n_u = 5 \times 5$, $n_p = 4 \times 3$

Figures 4–9 show the corresponding results, in which the red line stands for the value of β with respect to the number of pressure nodes n_p , and the vertical dashed line denotes the stabilized number n_s . The deeper color of the lines means mesh refinement. The results show that, no matter linear or quadratic elements, as n_p increases over n_s , the value of β sharply decreases, and then the inf-sup condition cannot be maintained. This result is consistent with the discussion in Section 3, and again verifies the effect of the proposed estimator.

Moreover, the mixed formulation's results with the traditional optimal constraint ratio $r = n_d$ are listed in these figures as well, and β in this circumstance is already much smaller than those in the optimal range. Considering the results shown above, the easy programming and efficiency, the pressure nodes are chosen among the displacement nodes. The optimal schemes for linear and quadratic, 2D and 3D element discretizations, namely with $r = r_{opt}$, are shown in Figure 10, where every other displacement node is selected as the pressure node. For practical implementations of linear cases, the pressure nodes are initially generated using traditional approaches, such as Delaunay triangulation. Subsequently, the displacement nodes are then obtained through a standard mesh refinement process to the pressure nodes. For quadratic approximations in Tri6 and Quad8 elements, the element vertices are chosen as pressure nodes after displacement element generation. Consequently, all constraint ratios evaluated using the discretizations in Figure 10 fall within the optimal range. The corresponding inf-sup test results for these schemes are also marked in inf-sup test figure and show that, with mesh refinement, their β 's are always maintained at a non-negligible level.

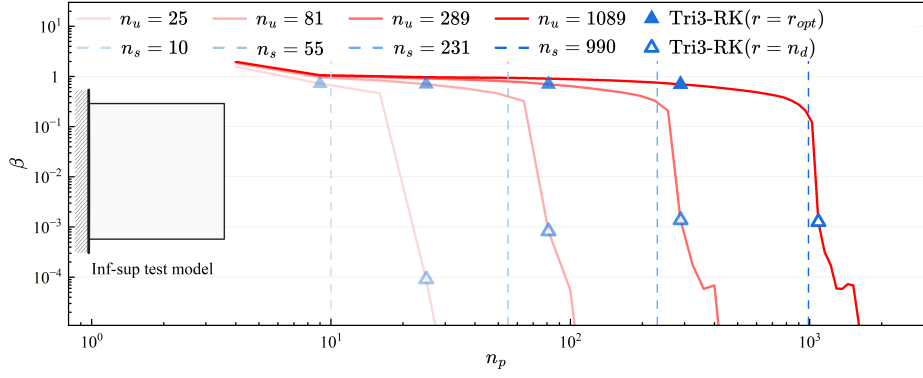


Figure 4: Inf-sup test for Tri3-RK

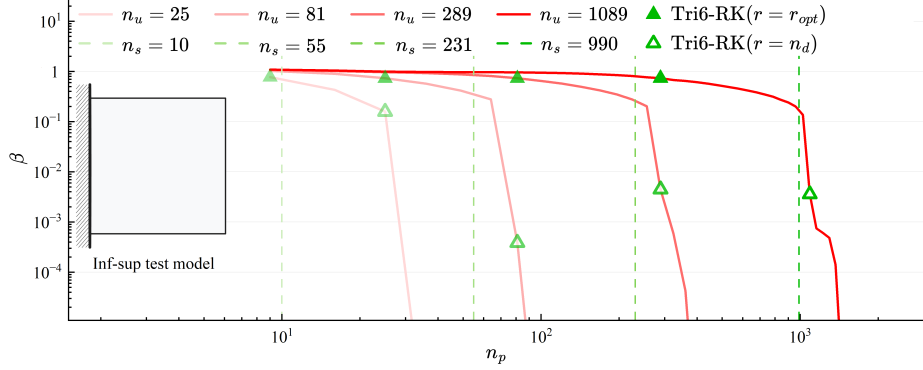


Figure 5: Inf-sup test for Tri6-RK

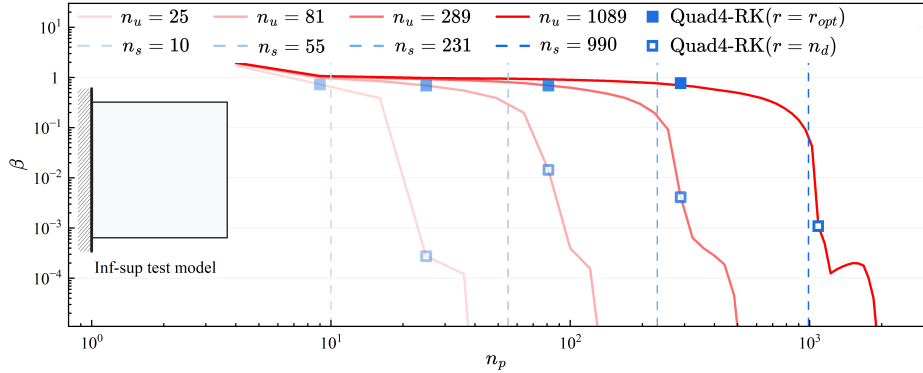


Figure 6: Inf-sup test for Quad4-RK

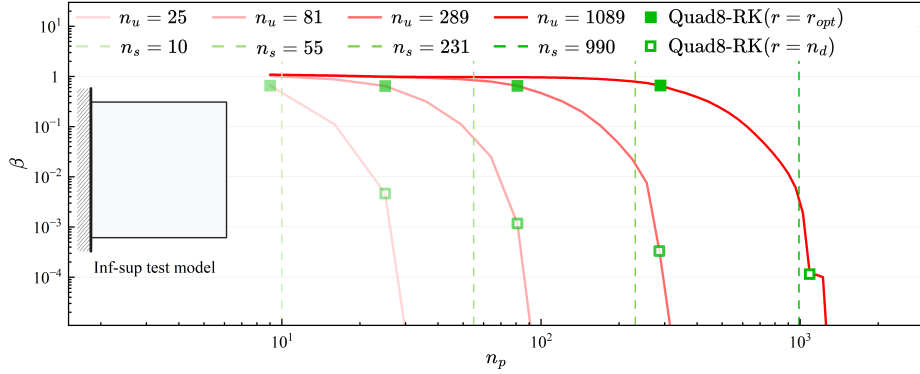


Figure 7: Inf-sup test for Quad8-RK

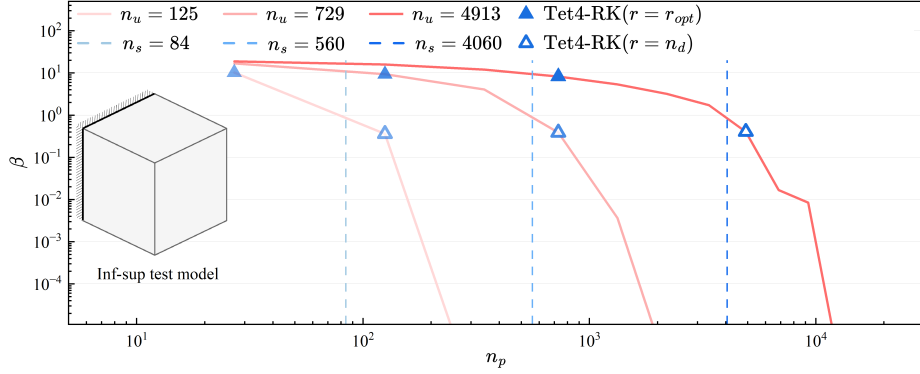
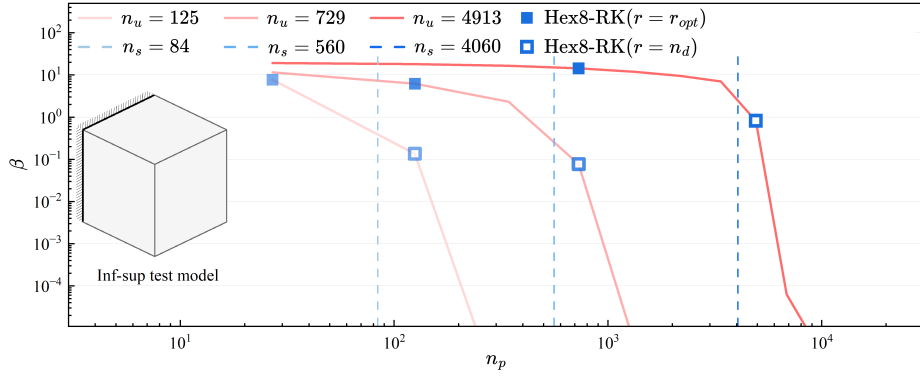


Figure 8: Inf-sup test for Tet4-RK



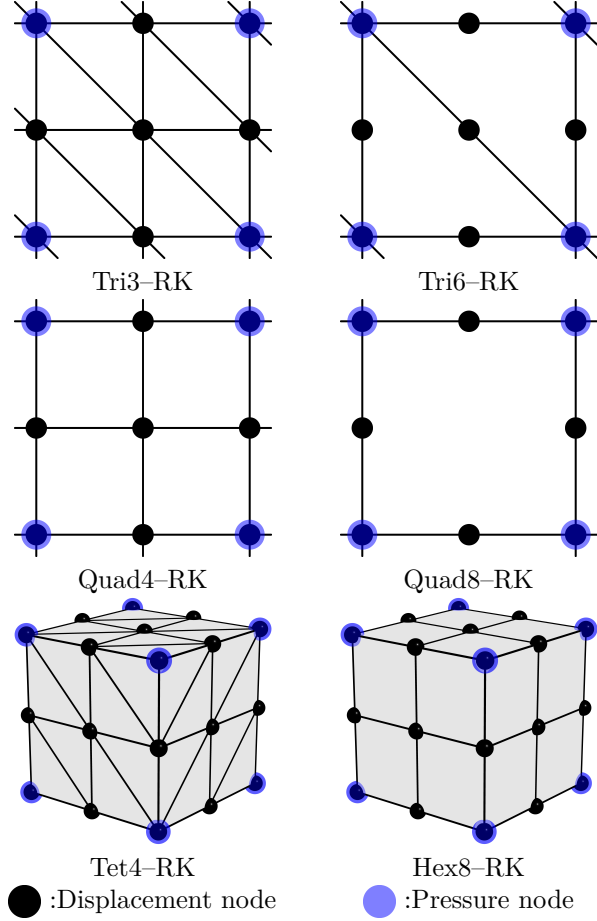


Figure 10: Nodal distribution schemes for mixed FE-meshfree formulations with $r = r_{opt}$

400 5. Numerical examples

401 5.1. Cantilever beam problem

402 Consider the cantilever beam problem shown in Figure 11 with length $L =$
403 $D = 12$, and the incompressible material parameters are employed
404 with Young's modulus $E = 3 \times 10^6$, Poisson's ratio $\nu = 0.5 - 10^{-8}$. The left hand
405 side is fixed and the right side subject to a concentrated force $P = 1000$. All
406 the prescribed values in the boundary conditions are evaluated by the analytical
407 solution that is given as follows [61]:

$$\begin{cases} u_x(\mathbf{x}) = -\frac{Py}{6EI} \left((6L - 3x)x + (2 + \bar{\nu})(y^2 - \frac{D^2}{4}) \right) \\ u_y(\mathbf{x}) = \frac{P}{6EI} \left(3\bar{\nu}y^2(L - x) + (4 + 5\bar{\nu})\frac{D^2x}{4} + (3L - x)x^2 \right) \end{cases} \quad (60)$$

⁴⁰⁸ where I is the beam's moment of inertia, \bar{E} and $\bar{\nu}$ are the material parameters
⁴⁰⁹ for plane strain hypothesis, they can be expressed by:

$$I = \frac{D^3}{12}, \quad \bar{E} = \frac{E}{1 - \nu^2}, \quad \bar{\nu} = \frac{\nu}{1 - \nu} \quad (61)$$

⁴¹⁰ And correspondingly, the stress components and the pressure are evaluated by

$$\begin{cases} \sigma_{xx} = -\frac{P(L-x)y}{I} \\ \sigma_{yy} = 0 \\ \sigma_{xy} = \frac{P}{2I}\left(\frac{D^2}{4} - y^2\right) \\ p = -\frac{P(1+\nu)(L-x)y}{3I} \end{cases} \quad (62)$$

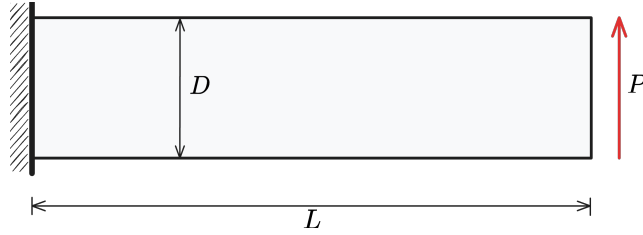


Figure 11: Illustration of cantilever beam problem

⁴¹¹ In this problem, the Tri3, Quad4 elements with 16×4 , 32×8 , 64×16 , 128×32
⁴¹² grids, and Tri6, Quad8 elements with 8×2 , 16×4 , 32×8 , 64×16 grids are
⁴¹³ employed for displacement discretization. The pressure is discretized by linear
⁴¹⁴ and quadratic meshfree approximations with 1.5 and 2.5 characterized support
⁴¹⁵ sizes respectively. The strain and pressure errors with respect to pressure nodes
⁴¹⁶ n_p are displayed in Figures 12, 13, where, to avoid the interpolation error, the
⁴¹⁷ pressure nodes are uniformly distributed independent with displacement nodes
⁴¹⁸ by the same way in Section 4.2. The vertical dashed lines stand for the stabilized
⁴¹⁹ number n_s . The figures imply that all pressure errors immediately increase when
⁴²⁰ their constraint ratios are out of the optimal range, and quadratic elements still
⁴²¹ have better results than linear elements. As n_p becomes very small, the pressure
⁴²² errors do not increase. This is because the pressure error estimator in Eq. (A.14)
⁴²³ is primarily controlled by the strain error and the inf-sup value β . The exact
⁴²⁴ pressure solution in Eq. (62) is only a second-order polynomial. As a result, the
⁴²⁵ pressure interpolation error in Eq. (A.14) is either very small or nonexistent.
⁴²⁶ For the strain error, the Quad8-RK method shows stable results regardless of
⁴²⁷ whether the constraint ratio is in the optimal range. This may be due to the
⁴²⁸ fact that the Quad8 element with a regular mesh satisfies the relationship of
⁴²⁹ Eq. (A.16). In this context, the strain error of Eq. (A.10) is independent of the
⁴³⁰ inf-sup value β and remains at a low level.

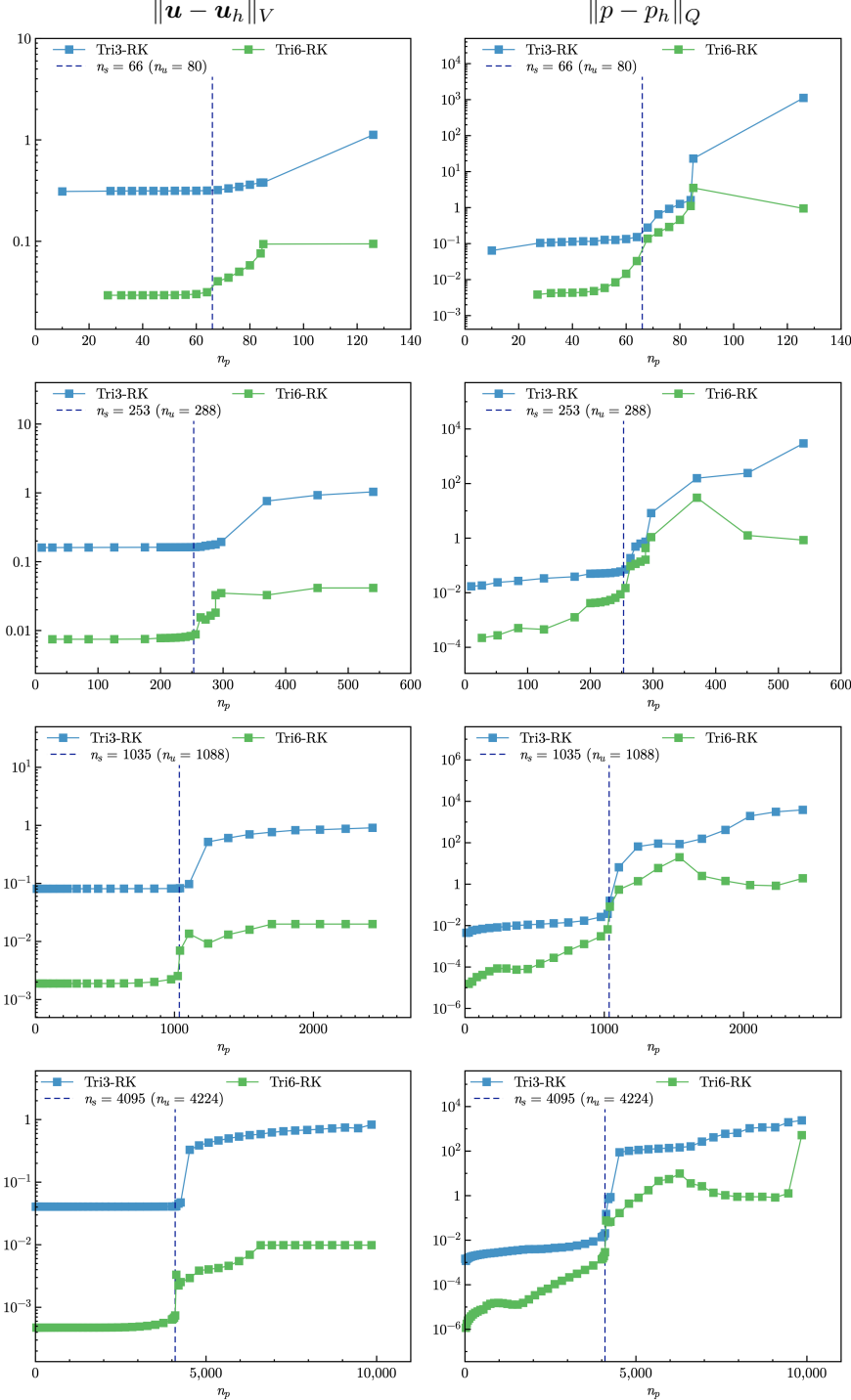


Figure 12: Strain and pressure errors vs. n_p for cantilever beam problem with triangular elements

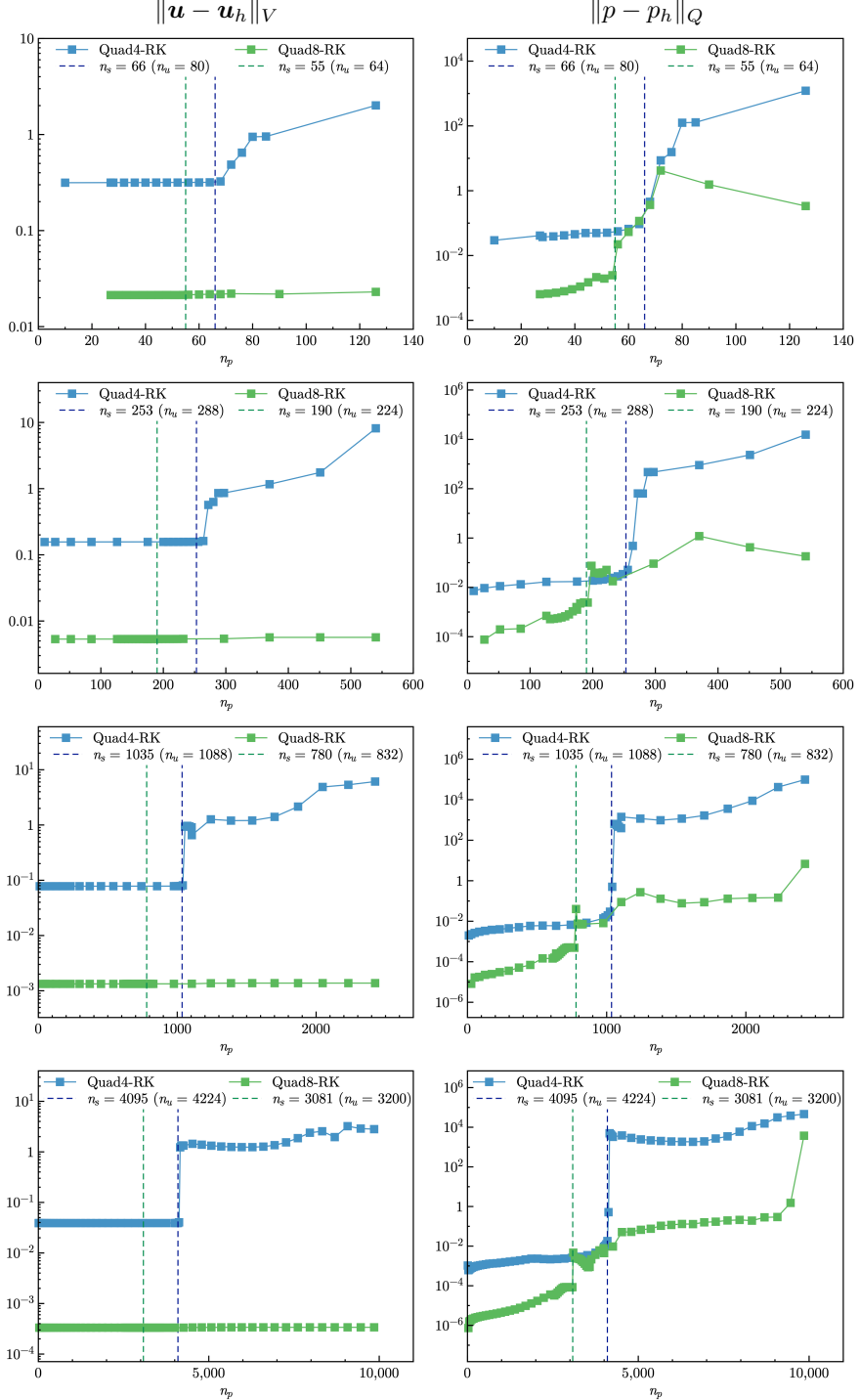


Figure 13: Strain and pressure errors vs. n_p for cantilever beam problem with quadrilateral elements

Additionally, a non-uniform discretization version of the study on strain and pressure errors with respect to n_p is conducted shown in Figure 14. To avoid the influence of the pressure interpolation error, the pressure nodes are still uniformly distributed, independent of the displacement nodes. The results in Figure 15 show that the pressure errors of linear approximations, Tri3–RK and Quad4–RK, immediately increase when their constraint ratios are outside the optimal range. The quadratic approximations, Tri6–RK and Quad8–RK, demonstrate better performance in resisting volumetric locking. In this case, the increase in pressure error has a gentler slope when the number of pressure nodes exceeds n_s .

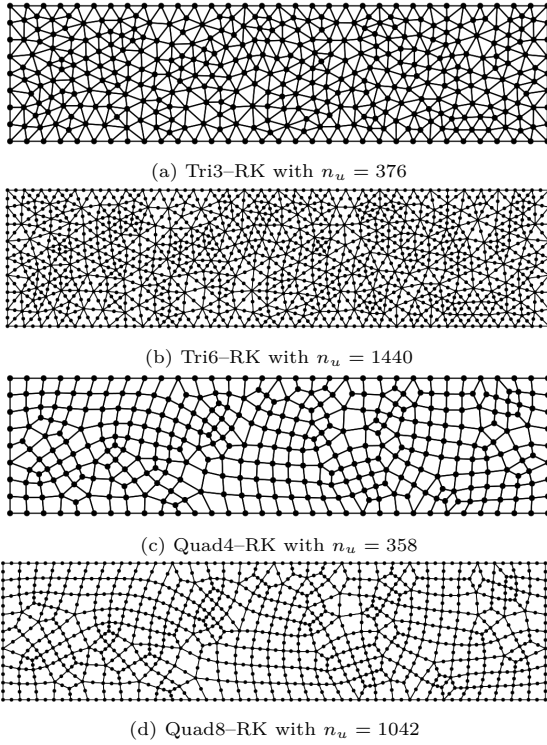


Figure 14: Non-uniform discretizations for cantilever beam problem

Figures 16, 17 are the strain and pressure error convergence studies for triangular and quadrilateral elements, respectively, in which Tri3–RK, Tri6–RK with $r = n_d$, the MINI element [32], 6-node triangular displacement element with 3-node continuous triangular pressure element (T6C3) are the comparative methods for Tri3–RK and Tri6–RK with $r = r_{opt}$, and Quad4–RK, Quad8–RK with $r = n_d$, 4-node quadrilateral displacement element with 1-node piecewise constant pressure (Q4P1), 8-node quadrilateral displacement element with 3-node piecewise linear pressure (Q8P3) are employed for comparison with Quad4–RK and Quad8–RK with $r = r_{opt}$. Except Tri3–RK, Quad8–RK with $r = n_d$

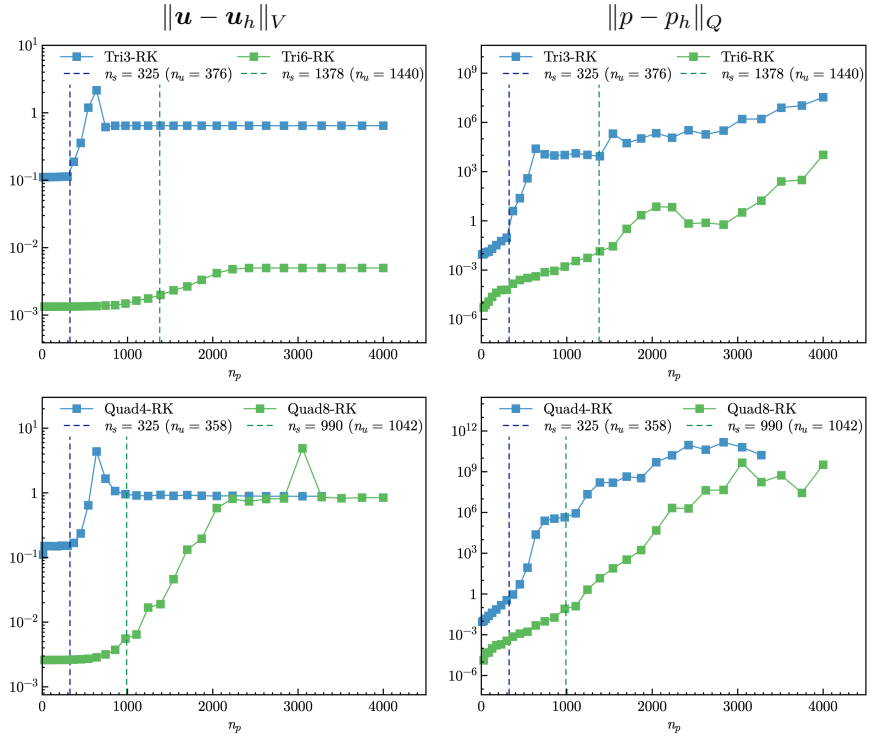


Figure 15: Strain and pressure errors vs. n_p for cantilever beam problem with non-uniform elements

for strain error, all formulations with the traditional constraint ratio of $r = n_d$ cannot ensure the optimal error convergence rates. The proposed mixed formulations with $r = r_{opt}$ can maintain the optimal error convergence ratio, except the strain error of Quad8-RK is a little larger than that of Q8P3, the proposed approaches show the best performance in accuracy.

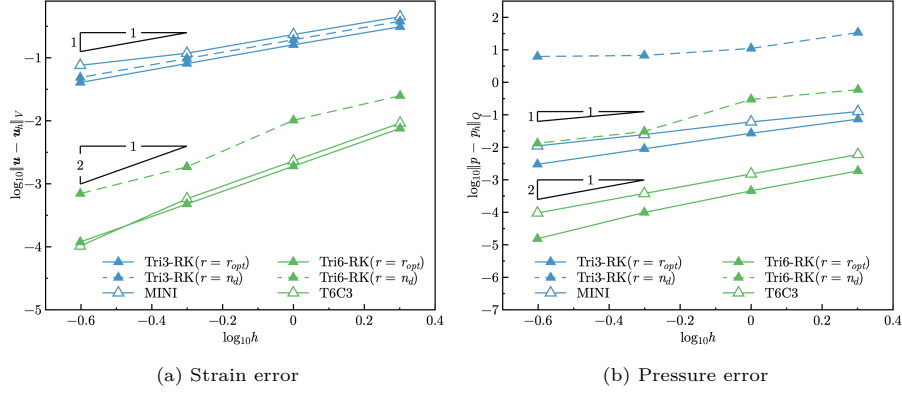


Figure 16: Error convergence study for cantilever beam problem with triangular elements

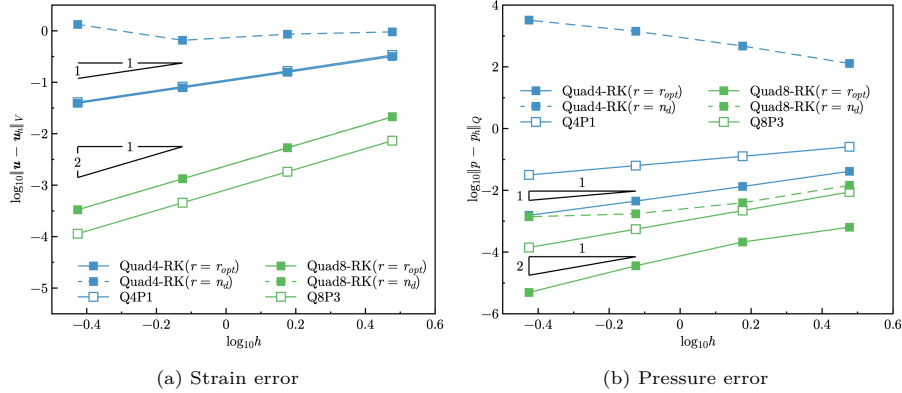


Figure 17: Error convergence study for cantilever beam problem with quadrilateral elements

455 5.2. Plate with hole problem

456 Consider an infinite plate with a hole centered at the origin, as shown in
457 Figure 18, and at the infinity towards the x -direction subjected to a uniform
458 traction $T = 1000$. The geometric and material parameters for this problem are
459 that the ratio of the hole $a = 1$, Young's modulus $E = 3 \times 10^6$, and Poisson's
460 ratio $\nu = 0.5 - 10^{-8}$. The analytical solution of this problem refers to the

⁴⁶¹ Michell solution [61] as:

$$\begin{cases} u_x(\rho, \theta) = \frac{Ta}{8\mu} \left(\frac{\rho}{a}(k+1) \cos \theta - \frac{2a^3}{\rho^3} \cos 3\theta + \frac{2a}{\rho} ((1+k) \cos \theta + \cos 3\theta) \right) \\ u_y(\rho, \theta) = \frac{Ta}{8\mu} \left(\frac{\rho}{a}(k-3) \sin \theta - \frac{2a^3}{\rho^3} \sin 3\theta + \frac{2a}{\rho} ((1-k) \sin \theta + \sin 3\theta) \right) \end{cases} \quad (63)$$

⁴⁶² in which $k = \frac{3-\nu}{1+\nu}$, $\mu = \frac{E}{2(1+\nu)}$. And the stress components are given by:

$$\begin{cases} \sigma_{xx} = T \left(1 - \frac{a^2}{\rho^2} \left(\frac{3}{2} \cos 2\theta + \cos 4\theta \right) + \frac{3a^4}{2\rho^4} \cos 4\theta \right) \\ \sigma_{yy} = -T \left(\frac{a^2}{\rho^2} \left(\frac{1}{2} \cos 2\theta - \cos 4\theta \right) + \frac{3a^4}{2\rho^4} \cos 4\theta \right) \\ \sigma_{xy} = -T \left(\frac{a^2}{\rho^2} \left(\frac{1}{2} \sin 2\theta + \sin 4\theta \right) - \frac{3a^4}{2\rho^4} \sin 4\theta \right) \end{cases} \quad (64)$$

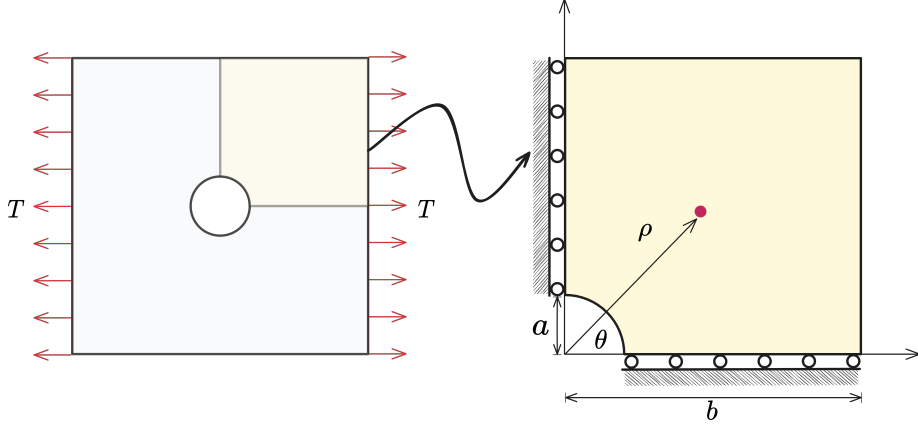


Figure 18: Illustration of plate with hole problem

⁴⁶³ According to the symmetry property of this problem, only a quarter model
⁴⁶⁴ with length $b = 5$ is considered as shown in Figure 18. The displacement is
⁴⁶⁵ discretized by 3-node, 6-node triangular elements, 4-node and 8-node quadrilateral
⁴⁶⁶ elements. The corresponding linear and quadratic meshfree formulations
⁴⁶⁷ are employed for pressure discretization, and the characterized support sizes
⁴⁶⁸ are chosen as 1.5 and 2.5, respectively. Figures 19, 20 study the relationship
⁴⁶⁹ between strain, pressure errors, and n_p using the nodal distributions uniformly
⁴⁷⁰ related to displacement nodes. Unlike the quadrilateral element case in Section
⁴⁷¹ 5.1, both displacement and pressure errors in this problem increase as n_p reduces
⁴⁷² to a small value. Tri3-RK exhibits less sensitivity in strain error than Tri6-RK.
⁴⁷³ This may be because, as shown in Eqs. (A.10) and (A.20), the displacement
⁴⁷⁴ approximation error for the space of $\ker \mathcal{P}_h$ does not increase as immediately

475 when $\frac{C_b}{\beta}$ in Eq. (A.20) is not too much larger than 1. However, its error in-
476 creases as n_p goes up. Both FE-RK with constraint ratios under the optimal
477 range perform acceptably.

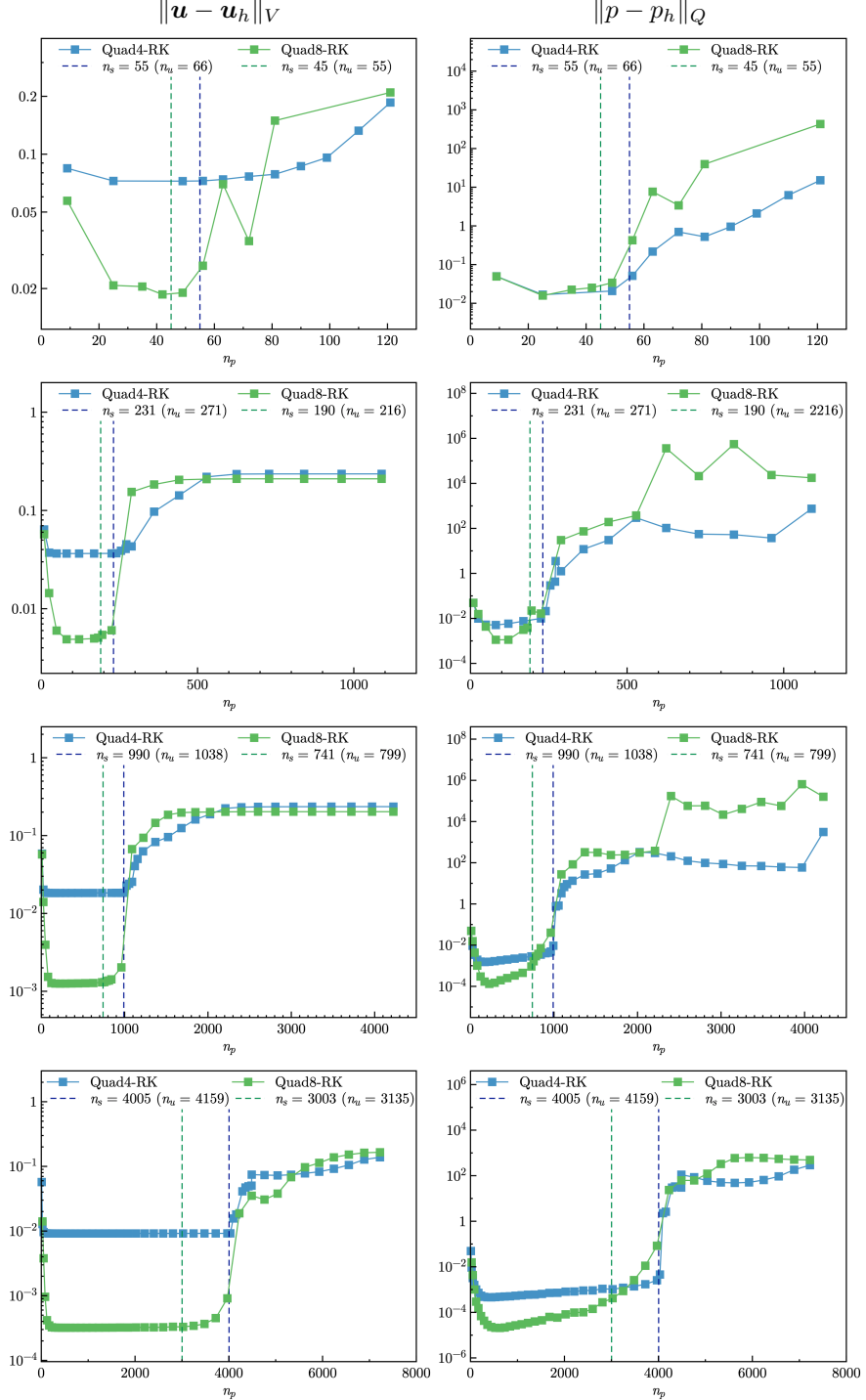


Figure 20: Strain and pressure errors vs. n_p for plate with hole problem

478 The corresponding error convergence studies are presented in Figures 21, 22,
 479 the results show that only Tri3–RK with $r = 2$ shows a comparable result with
 480 the optimal one with $r = r_{opt}$ in strain error. The other formulations with the
 481 traditional constraint ratio show lower accuracy and error convergence rates.

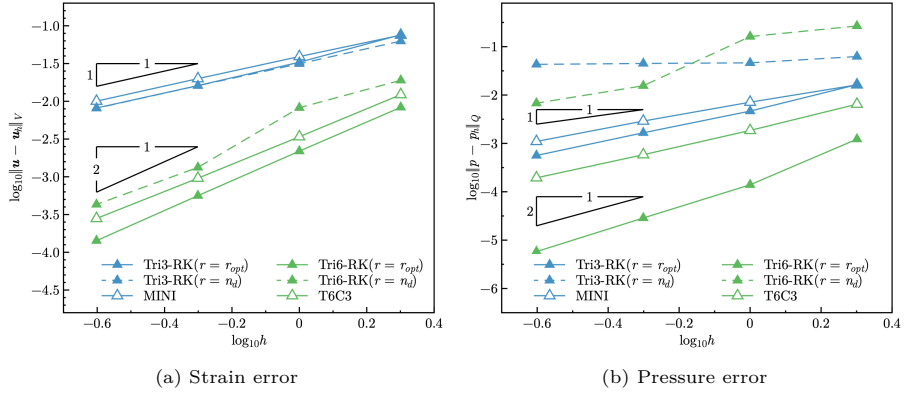


Figure 21: Error convergence study for plate with a hole problem with triangular elements

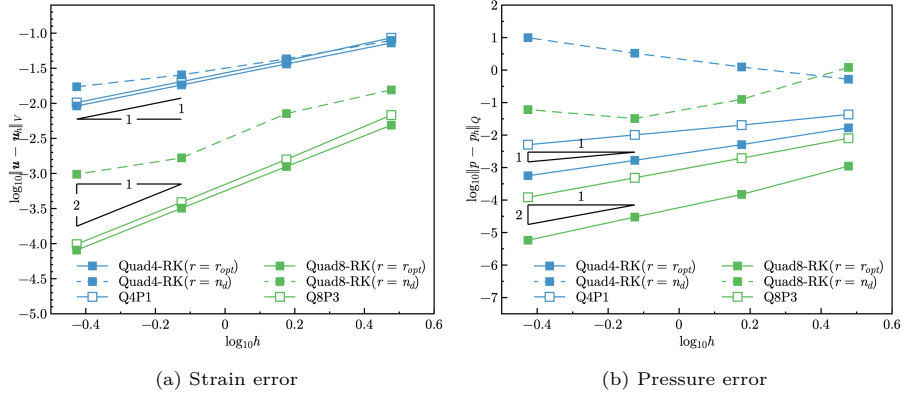


Figure 22: Error convergence study for plate with a hole problem with quadrilateral elements

482 Furthermore, the influence of the integration scheme for this problem is
 483 investigated. As shown in Tables 3 and 4, the integration order n_o is varied
 484 from 1 to 5 for triangular elements and from 1 to 11 for quadrilateral elements.
 485 The results show that the proposed mixed formulations are not sensitive to the
 486 integration order. Using the traditional lower-order Gauss integration scheme
 487 can sufficiently obtain accurate results. This is consistent with the previous
 488 analysis in Section 4.1.

Table 3: Error comparison with different triangular integration schemes for plate with a hole problem

n_o	n_g for Ω	n_g for Γ	Tri3-RK		Tri6-RK	
			$\ \mathbf{u} - \mathbf{u}_h\ _V$	$\ p - p_h\ _Q$	$\ \mathbf{u} - \mathbf{u}_h\ _V$	$\ p - p_h\ _Q$
1	1	1	3.11E-2	3.53E-3	8.53E17	1.31E4
2	3	2	3.11E-2	3.67E-3	8.33E-3	1.20E-3
3	4	2	3.11E-2	3.67E-3	8.32E-3	1.20E-3
4	6	3	3.11E-2	3.68E-3	8.32E-3	1.22E-3
5	7	3	3.11E-2	3.68E-3	8.32E-3	1.22E-3

n_o : Integration order n_g : Number of integration points

Table 4: Error comparison with different quadrilateral integration schemes for plate with a hole problem

n_o	n_g for Ω	n_g for Γ	Quad4-RK		Quad8-RK	
			$\ \mathbf{u} - \mathbf{u}_h\ _V$	$\ p - p_h\ _Q$	$\ \mathbf{u} - \mathbf{u}_h\ _V$	$\ p - p_h\ _Q$
1	3	1	3.64E-2	5.01E-3	9.53E13	8.15E-1
3	2×2	2	3.64E-2	5.09E-3	4.33E-2	8.84E-3
5	3×3	3	3.62E-2	3.71E-3	1.27E-3	4.42E-5
7	4×4	4	3.62E-2	3.70E-3	1.26E-3	1.49E-4
9	5×5	5	3.62E-2	3.70E-3	1.26E-3	1.50E-4
11	6×6	6	3.62E-2	3.70E-3	1.26E-3	1.50E-4

n_o : Integration Order n_g : Number of integration points

489 5.3. Cook's membrane problem

490 The Cook's membrane problem [12] is used herein for stability analysis of
491 pressure. The geometry of this problem is shown in Figure 23, in which the left
492 hand side is fixed and the right hand side subjects a concentrated force $P = 6.25$
493 in the y -direction. The material parameters are Young's modulus $E = 70.0$ and
494 Poisson's ratio $\nu = 0.5 - 10^{-8}$.

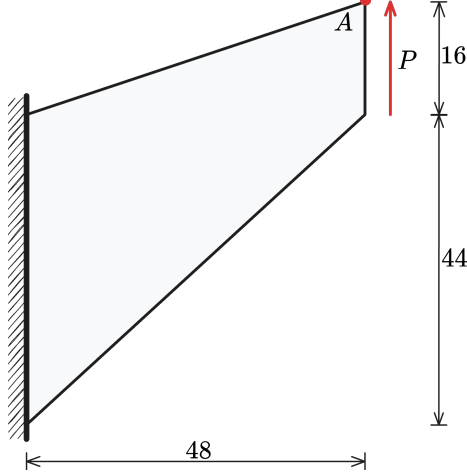


Figure 23: Illustration of Cook's membrane problem

In this test, we evaluated the convergence properties by comparing the vertical displacement at point A against a reference value of 28.0. As shown in Figure 24 illustrates, the methods employing $r = r_{opt}$ produced results that were notably closer to this reference value than those using $r = n_d$. Furthermore, to investigate stability, Figures 25–28 show the pressure contour plots for non-uniform Tri3–RK, Tri6–RK, Quad4–RK, and Quad8–RK formulations with $r = n_d$ and $r = r_{opt}$, respectively. The reproducing kernel meshfree approximations are employed for pressure discretization with characterized support sizes of 1.5 for the linear basis function and 2.5 for the quadratic basis function. The results imply that the pressure contour plots with the optimal constraint ratio $r = r_{opt}$ show a more stable and smooth pressure distribution compared to those with the traditional constraint ratio $r = n_d$.

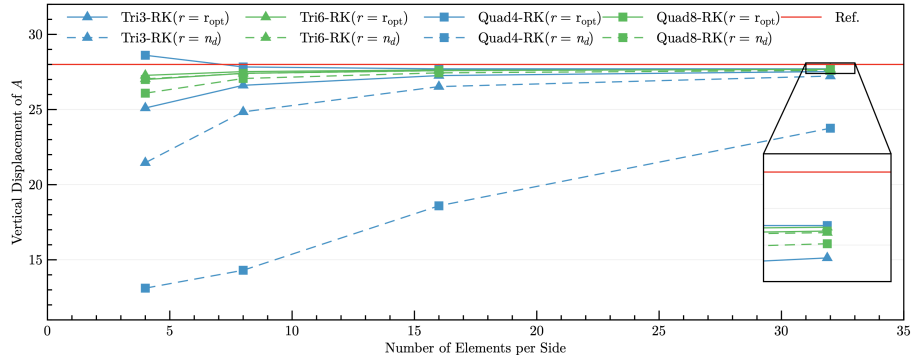


Figure 24: Convergence comparison of the vertical displacement at point A for Cook's membrane problem

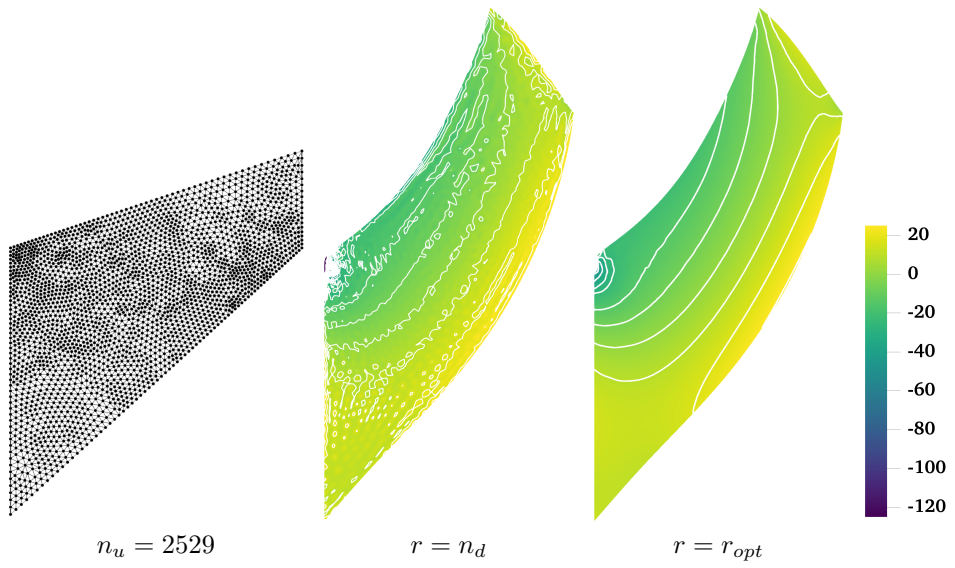


Figure 25: Pressure contour plots for Cook's membrane problem using Tri3–RK

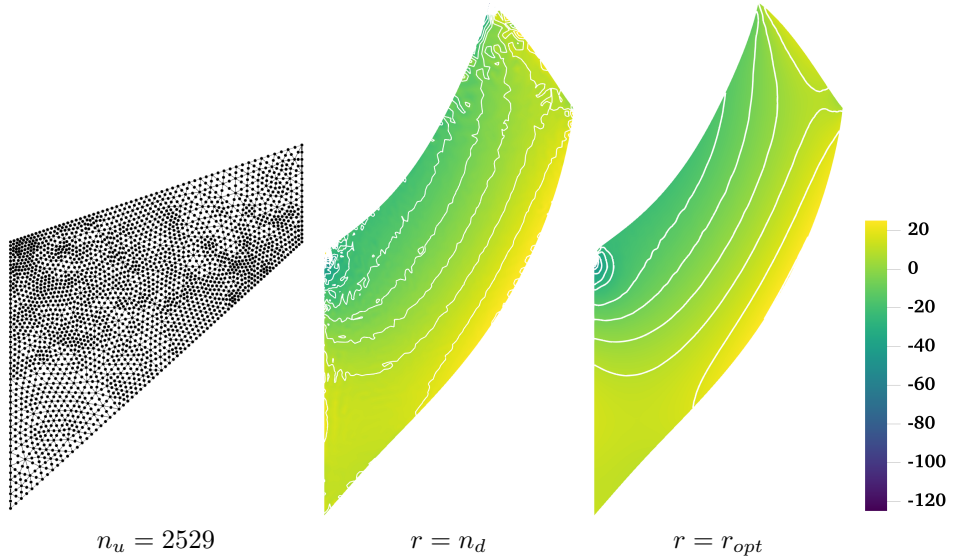


Figure 26: Comparison of pressure contour plots for Cook's membrane problem using Tri6–RK

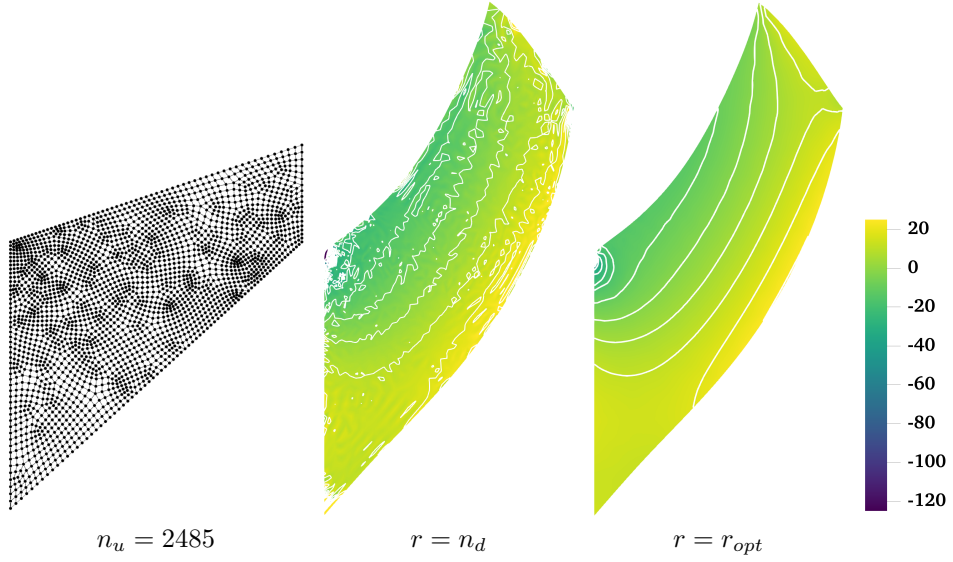


Figure 27: Comparison of pressure contour plots for Cook's membrane problem using Quad4–RK

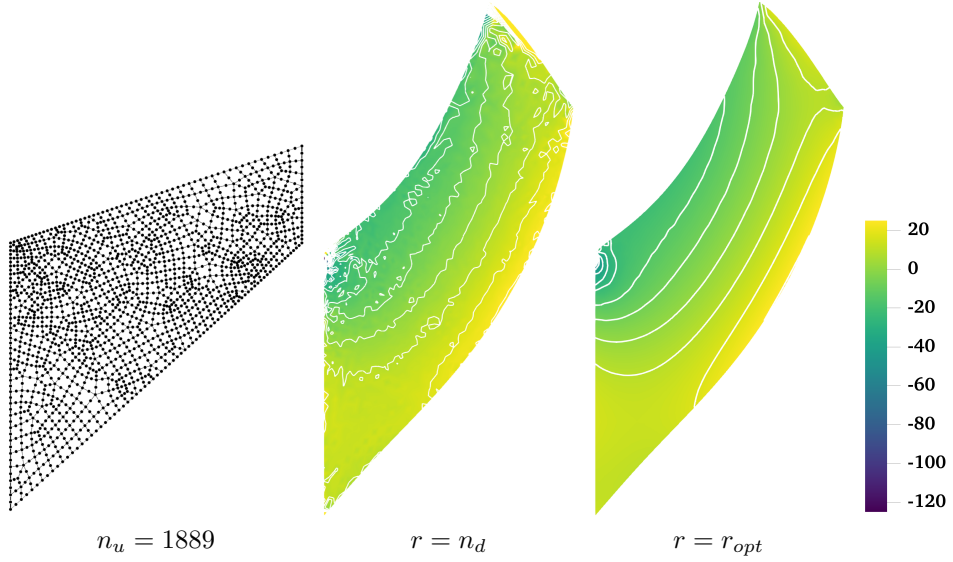


Figure 28: Comparison of pressure contour plots for Cook's membrane problem using Quad8–RK

507 An efficiency comparison of different methods for the Cook's membrane prob-
 508 lem is presented in Table 5. This includes the condition number of the global
 509 stiffness matrix and the CPU time for shape function construction, system as-

510 sembly, and system solving. The mixed FE–Meshfree formulations spend more
 511 time compared to the traditional element–based formulations. This is mainly
 512 due to the implicit, complicated expression of meshfree shape functions and the
 513 larger bandwidth of the stiffness matrix, which results from the larger support
 514 size of the meshfree shape functions.

Table 5: Condition number and efficiency comparison for Cook’s membrane problem

Method	Condition number	CPU–time (s) for		
		Shape function	Assembly	Solving
MINI	1.11E06	0.025	0.327	0.022
Tri3–RK($r = n_d$)	1.89E10	1.730	4.160	0.108
Tri3–RK($r = r_{opt}$)	1.13E08	1.290	1.720	0.052
T6C3	1.62E05	0.004	0.380	0.021
Tri6–RK($r = n_d$)	2.48E16	1.620	1.670	0.294
Tri6–RK($r = r_{opt}$)	3.69E10	1.110	0.634	0.077
Q4P1	5.75E12	0.011	0.344	0.021
Quad4–RK($r = n_d$)	5.21E10	2.100	4.890	0.122
Quad4–RK($r = r_{opt}$)	1.97E08	1.500	2.140	0.057
Q8P3	2.69E07	0.005	0.373	0.015
Quad8–RK($r = n_d$)	2.75E15	1.170	1.180	0.184
Quad8–RK($r = r_{opt}$)	8.67E10	0.847	0.471	0.065

515 5.4. Block under compression problem

516 The incompressible block problem [62] shown in Figure 29 is considered for
 517 testing 3D mixed formulations. The block’s dimensions are $2L \times 2L \times L$, $L = 1$.
 518 At the center of the top surface of the block is applied a pressure load P with
 519 the area of $L \times L$. Due to the symmetry of this problem, only a quarter model is
 520 considered. The Young’s modulus and Poisson’s ratio are set as $E = 240.56839$
 521 and $\nu = 0.5 - 10^{-8}$, respectively.

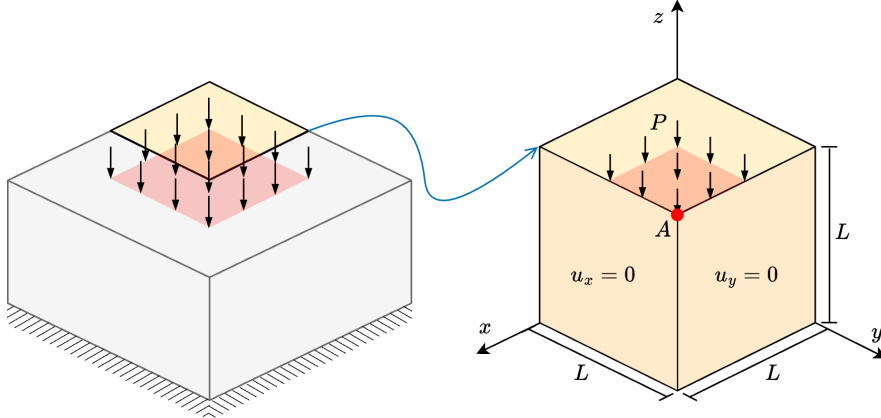


Figure 29: Illustration of block under compression problem

522 The convergence properties of the mixed formulations are evaluated by com-
 523 paring the compression level at point A under loading condition $P = 80$. As
 524 shown in Figure 30, all the results exhibit good convergence behavior across
 525 different loading levels. Figures 31, 32 study the pressure stability of 3D mixed
 526 FE-meshfree formulations, Tet4-RK and Hex8-RK, with non-uniform nodal
 527 distribution, while the pressure is discretized by linear meshfree approximations
 528 with a characterized support size of 1.5. The corresponding results also show
 529 the well performance of the proposed optimal constraint ratio $r = r_{opt}$. The
 530 mixed formulations with the traditional constraint ratio $r = n_d$ show compara-
 531 ble displacement results, but exhibit significant pressure instability.

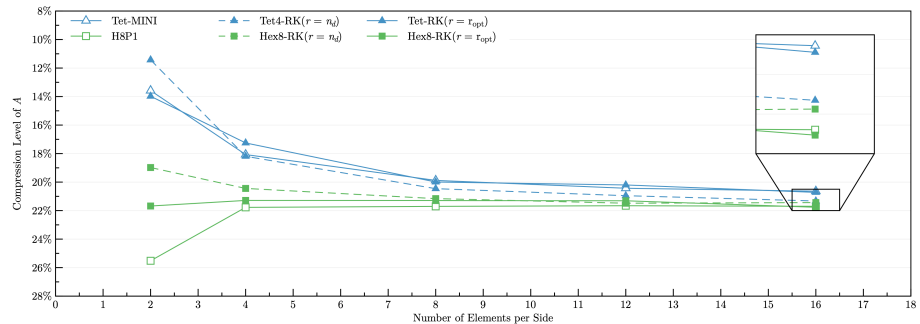


Figure 30: Convergence comparison of compression level (%) at point A for block under compression problem

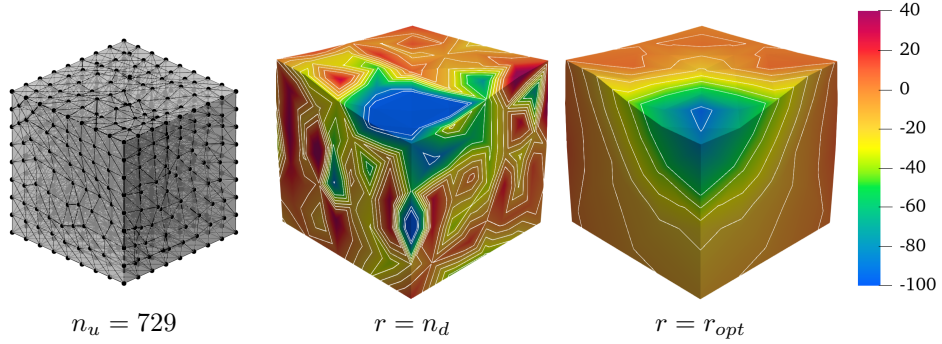


Figure 31: Comparison of pressure contour plots for block under compression problem using Tet4–RK

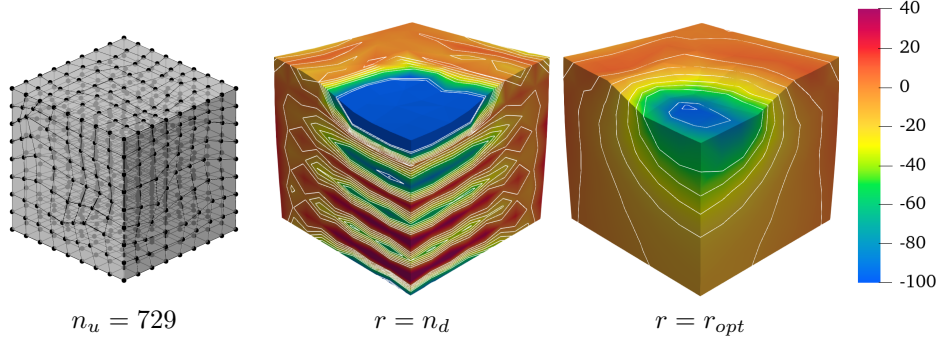


Figure 32: Comparison of pressure contour plots for block under compression problem using Hex8–RK

532 6. Conclusion

533 This paper proposes a novel optimal constraint ratio derived from the inf–sup
 534 condition to address volumetric locking. The optimal constraint ratio requires
 535 that, for a given number of displacement DOFs, the number of pressure DOFs
 536 should remain below a stabilized number determined by the proposed inf–sup
 537 value estimator. For a well-posed nodal distribution, simply counting the dis-
 538 placement and pressure DOFs can determine whether the formulation satisfies
 539 the inf–sup condition. Compared to the traditional constraint ratio, the pro-
 540 posed ratio is theoretically grounded in the inf–sup condition and thus is more
 541 precise, and it also provides a simple way to justify the satsification of inf–sup
 542 conditiion just by counting the DOFs of displacement and pressure fields.

543 To implement this constraint ratio, a mixed finite element (FE) and meshfree
 544 formulation is developed. Displacements are discretized using 3-node and 6-node
 545 triangular elements, 4-node and 8-node quadrilateral elements in 2D, and 4-node
 546 tetrahedral and 8-node hexahedral elements in 3D. Correspondingly, linear and

547 quadratic reproducing kernel meshfree approximations are used for pressure
548 discretization. The reproducing kernel approximation equips globally smooth
549 shape functions, allowing arbitrary pressure DOF placement without the limit
550 of element. However, the implicit expression of shape functions and the larger
551 bandwidth of the stiffness matrix in meshfree approximation also lead to larger
552 condition number and lower efficiency compared with traditional element-based
553 formulations.

554 Inf-sup tests for mixed FE-meshfree formulations with different constraint
555 ratios verify the effectiveness of the proposed inf-sup value estimator. For effi-
556 ciency and ease of implementation, the final nodal distribution scheme selects
557 every other displacement node as a pressure node, ensuring the optimal con-
558 straint ratio and satisfying the inf-sup condition.

559 A series of 2D and 3D incompressible elasticity examples demonstrate the
560 effectiveness of the proposed mixed formulation. Results show that formulations
561 with the optimal constraint ratio yield accurate displacement and pressure solu-
562 tions. When the constraint ratio exceeds the optimal value, errors rise sharply
563 to unacceptable levels, with the 8-node quadrilateral element being the only
564 exception that maintains good displacement accuracy. Error convergence stud-
565 ies and pressure contour plots further confirm that mixed formulations with
566 the optimal constraint ratio achieve optimal convergence rates and effectively
567 suppress pressure oscillations.

568 Acknowledgment

569 The support of this work by the National Natural Science Foundation of
570 China (12102138), the Natural Science Foundation of Fujian Province of China
571 (2023J01108) and the Fundamental Research Funds of Central Universities
572 (ZQN-1014) is gratefully acknowledged.

573 References

- 574 [1] F. Brezzi, M. Fortin, Mixed and Hybrid Finite Element Methods, Vol. 15 of
575 Springer Series in Computational Mathematics, Springer, New York, NY,
576 1991.
- 577 [2] T. J. Hughes, The Finite Element Method: Linear Static and Dynamic
578 Finite Element Analysis, Prentice Hall, New Jersey, 2000.
- 579 [3] I. Babuška, R. Narasimhan, The Babuška-Brezzi condition and the patch
580 test: An example, Computer Methods in Applied Mechanics and Engineering
581 140 (1-2) (1997) 183–199.
- 582 [4] K. J. Bathe, Finite Element Procedures, Prentice Hall, Englewood Cliffs,
583 New Jersey, 1996.
- 584 [5] D. S. Malkus, Eigenproblems associated with the discrete LBB condition for
585 incompressible finite elements, International Journal of Engineering Science
586 19 (10) (1981) 1299–1310.

- 587 [6] D. Chapelle, K. J. Bathe, The inf-sup test, Computers & Structures 47 (4)
588 (1993) 537–545.
- 589 [7] F. Brezzi, K. J. Bathe, Studies of finite element procedures the inf-sup
590 condition equivalent forms and applications.
- 591 [8] D. Gallistl, Rayleigh-Ritz approximation of the inf-sup constant for the
592 divergence, Mathematics of Computation 88 (315) (2019) 73–89.
- 593 [9] P. Hood, C. Taylor, Navier-Stokes equations using mixed interpolation,
594 Finite element methods in flow problems (1974) 121–132.
- 595 [10] D. S. Malkus, T. J. Hughes, Mixed finite element methods - Reduced and
596 selective integration techniques: A unification of concepts, Computer Meth-
597 ods in Applied Mechanics and Engineering 15 (1) (1978) 63–81.
- 598 [11] T. Shilt, R. Deshmukh, J. J. McNamara, P. J. O'Hara, Solution of nearly
599 incompressible field problems using a generalized finite element approach,
600 Computer Methods in Applied Mechanics and Engineering 368 (2020)
601 113165.
- 602 [12] J. C. Simo, M. S. Rifai, A class of mixed assumed strain methods and
603 the method of incompatible modes, International Journal for Numerical
604 Methods in Engineering 29 (8) (1990) 1595–1638.
- 605 [13] M. Broccardo, M. Micheloni, P. Krysl, Assumed-deformation gradient finite
606 elements with nodal integration for nearly incompressible large deformation
607 analysis, International Journal for Numerical Methods in Engineering 78 (9)
608 (2009) 1113–1134.
- 609 [14] W. M. Coombs, T. J. Charlton, M. Cortis, C. E. Augarde, Overcoming vol-
610 umetric locking in material point methods, Computer Methods in Applied
611 Mechanics and Engineering 333 (2018) 1–21.
- 612 [15] S. Saloustros, M. Cervera, S. Kim, M. Chiumenti, Accurate and locking-free
613 analysis of beams, plates and shells using solid elements, Computational
614 Mechanics 67 (2021) 883–914.
- 615 [16] J. Simo, R. Taylor, K. Pister, Variational and projection methods for the
616 volume constraint in finite deformation elasto-plasticity, Computer Meth-
617 ods in Applied Mechanics and Engineering 51 (1-3) (1985) 177–208.
- 618 [17] C. R. Dohrmann, P. B. Bochev, A stabilized finite element method for the
619 Stokes problem based on polynomial pressure projections, International
620 Journal for Numerical Methods in Fluids 46 (2) (2004) 183–201.
- 621 [18] A. Valverde-González, J. Reinoso, B. Dorddivanlioglu, M. Paggi, Locking
622 treatment of penalty-based gradient-enhanced damage formulation for fail-
623 ure of compressible and nearly incompressible hyperelastic materials, Com-
624 putational Mechanics 72 (2023) 635–662.

- 625 [19] B.-B. Xu, F. Peng, P. Wriggers, Stabilization-free virtual element method
 626 for finite strain applications, Computer Methods in Applied Mechanics and
 627 Engineering 417 (2023) 116555.
- 628 [20] F. S. Liguori, A. Madeo, S. Marfia, G. Garcea, E. Sacco, A stabilization-
 629 free hybrid virtual element formulation for the accurate analysis of 2D
 630 elasto-plastic problems, Computer Methods in Applied Mechanics and En-
 631 gineering 431 (2024) 117281.
- 632 [21] R. Alves de Sousa, R. Natal Jorge, R. Fontes Valente, J. César de Sá, A new
 633 volumetric and shear locking-free 3D enhanced strain element, Engineering
 634 Computations 20 (7) (2003) 896–925.
- 635 [22] K.-J. Bathe, The inf-sup condition and its evaluation for mixed finite ele-
 636 ment methods, Computers & Structures 79 (2) (2001) 243–252.
- 637 [23] T. J. R. Hughes, Multiscale phenomena: Green's functions, the Dirichlet-
 638 to-Neumann formulation, subgrid scale models, bubbles and the origins of
 639 stabilized methods, Computer Methods in Applied Mechanics and Engi-
 640 neering 127 (1) (1995) 387–401.
- 641 [24] R. Rossi, R. Zorrilla, R. Codina, A stabilised displacement-volumetric
 642 strain formulation for nearly incompressible and anisotropic materials,
 643 Computer Methods in Applied Mechanics and Engineering 377 (2021)
 644 113701.
- 645 [25] E. Karabelas, M. A. F. Gsell, G. Haase, G. Plank, C. M. Augustin, An
 646 accurate, robust, and efficient finite element framework with applications to
 647 anisotropic, nearly and fully incompressible elasticity, Computer Methods
 648 in Applied Mechanics and Engineering 394 (2022) 114887.
- 649 [26] R. Codina, I. Castañar, J. Baiges, Finite element approximation of stabi-
 650 lized mixed models in finite strain hyperelasticity involving displace-
 651 ments and stresses and/or pressure—An overview of alternatives, International
 652 Journal for Numerical Methods in Engineering (2024) e7540.
- 653 [27] L. Moreno, R. Wuechner, A. Larese, A mixed stabilized MPM formula-
 654 tion for incompressible hyperelastic materials using Variational Subgrid-
 655 Scales, Computer Methods in Applied Mechanics and Engineering 435
 656 (2025) 117621.
- 657 [28] T. J. R. Hughes, L. P. Franca, M. Balestra, A new finite element formu-
 658 lation for computational fluid dynamics: V. Circumventing the babuška-
 659 brezzi condition: A stable Petrov-Galerkin formulation of the stokes prob-
 660 lem accommodating equal-order interpolations, Computer Methods in Ap-
 661 plied Mechanics and Engineering 59 (1) (1986) 85–99.
- 662 [29] A. N. Brooks, T. J. R. Hughes, Streamline upwind/Petrov-Galerkin formu-
 663 lations for convection dominated flows with particular emphasis on the in-
 664 compressible Navier-Stokes equations, Computer Methods in Applied Me-
 665 chanics and Engineering 32 (1) (1982) 199–259.

- 666 [30] L. He, L. Jing, M. Feng, New stabilized mixed finite element methods for
 667 two-field poroelasticity with low permeability, *Applied Mathematics and*
 668 *Computation* 494 (2025) 129285.
- 669 [31] D. N. Arnold, F. Brezzi, M. Fortin, A stable finite element for the Stokes
 670 equations, *CALCOLO* 21 (4) (1984) 337–344.
- 671 [32] F. Auricchio, L. Beirão da Veiga, C. Lovadina, A. Reali, A stability study of
 672 some mixed finite elements for large deformation elasticity problems, *Computer*
 673 *Methods in Applied Mechanics and Engineering* 194 (9-11) (2005)
 674 1075–1092.
- 675 [33] A. Quarteroni, A. Valli, *Numerical Approximation of Partial Differential*
 676 *Equations*, Springer Series in Computational Mathematics, Springer,
 677 Berlin, 1994.
- 678 [34] M. Crouzeix, P. Raviart, Conforming and nonconforming finite ele-
 679 ment methods for solving the stationary Stokes equations I, *Revue*
 680 *française d'automatique informatique recherche opérationnelle. Mathéma-*
 681 *tique* 7 (R3) (1973) 33–75.
- 682 [35] U. Brink, E. Stein, On some mixed finite element methods for incompress-
 683 ible and nearly incompressible finite elasticity, *Computational Mechanics*
 684 19 (1) (1996) 105–119.
- 685 [36] T. Belytschko, Y. Y. Lu, L. Gu, Element-free Galerkin methods, *Internation-
 686 al Journal for Numerical Methods in Engineering* 37 (2) (1994) 229–256.
- 687 [37] W. K. Liu, S. Jun, Y. F. Zhang, Reproducing kernel particle methods, *Internation-
 688 al Journal for Numerical Methods in Fluids* 20 (8-9) (1995) 1081–
 689 1106.
- 690 [38] C. Rodriguez, T.-H. Huang, A variationally consistent reproducing ker-
 691 nel enhanced material point method and its applications to incompressible
 692 materials, *Computational Mechanics* (2023) 1–20.
- 693 [39] S. W. Chi, J. S. Chen, H. Y. Hu, A weighted collocation on the strong form
 694 with mixed radial basis approximations for incompressible linear elasticity,
 695 *Computational Mechanics* 53 (2) (2014) 309–324.
- 696 [40] L. Wang, Z. Qian, Y. Zhou, Y. Peng, A weighted meshfree collocation
 697 method for incompressible flows using radial basis functions, *Journal of*
 698 *Computational Physics* 401 (2020) 108964.
- 699 [41] A. Ortiz-Bernardin, M. Puso, N. Sukumar, Improved robustness for nearly-
 700 incompressible large deformation meshfree simulations on Delaunay tes-
 701 sellations, *Computer Methods in Applied Mechanics and Engineering* 293
 702 (2015) 348–374.

- 703 [42] T. J. Hughes, J. A. Cottrell, Y. Bazilevs, Isogeometric analysis: CAD,
 704 finite elements, NURBS, exact geometry and mesh refinement, Computer
 705 Methods in Applied Mechanics and Engineering 194 (39-41) (2005) 4135–
 706 4195.
- 707 [43] F. Auricchio, L. Beirão da Veiga, C. Lovadina, A. Reali, The importance
 708 of the exact satisfaction of the incompressibility constraint in nonlinear
 709 elasticity: Mixed FEMs versus NURBS-based approximations, Computer
 710 Methods in Applied Mechanics and Engineering 199 (5) (2010) 314–323.
- 711 [44] A. Huerta, S. Fernández-Méndez, Locking in the incompressible limit for
 712 the element-free Galerkin method, International Journal for Numerical
 713 Methods in Engineering 51 (11) (2001) 1361–1383.
- 714 [45] J. Dolbow, T. Belytschko, Volumetric locking in the element free Galerkin
 715 method, International Journal for Numerical Methods in Engineering 46 (6)
 716 (1999) 925–942.
- 717 [46] G. Moutsanidis, J. J. Koester, M. R. Tupek, J.-S. Chen, Y. Bazilevs, Treat-
 718 ment of near-incompressibility in meshfree and immersed-particle methods,
 719 Computational Particle Mechanics 7 (2) (2020) 309–327.
- 720 [47] G. Moutsanidis, W. Li, Y. Bazilevs, Reduced quadrature for FEM, IGA
 721 and meshfree methods, Computer Methods in Applied Mechanics and En-
 722 gineering 373 (2021) 113521.
- 723 [48] Z.-Y. Wang, Y.-F. Jin, Z.-Y. Yin, Y.-Z. Wang, Overcoming volumetric
 724 locking in stable node-based smoothed particle finite element method with
 725 cubic bubble function and selective integration, International Journal for
 726 Numerical Methods in Engineering 123 (24) (2022) 6148–6169.
- 727 [49] T. Elguedj, Y. Bazilevs, V. Calo, T. Hughes, B[−] and F[−] projection meth-
 728 ods for nearly incompressible linear and non-linear elasticity and plasticity
 729 using higher-order NURBS elements, Computer Methods in Applied Me-
 730 chanics and Engineering 197 (33-40) (2008) 2732–2762.
- 731 [50] J. S. Chen, S. Yoon, H. P. Wang, W. K. Liu, An improved reproducing
 732 kernel particle method for nearly incompressible finite elasticity, Computer
 733 Methods in Applied Mechanics and Engineering 181 (1) (2000) 117–145.
- 734 [51] C. M. Goh, P. M. F. Nielsen, M. P. Nash, A stabilised mixed mesh-
 735 free method for incompressible media: Application to linear elasticity and
 736 Stokes flow, Computer Methods in Applied Mechanics and Engineering 329
 737 (2018) 575–598.
- 738 [52] D. S. Bombarde, M. Agrawal, S. S. Gautam, A. Nandy, Hellinger–Reissner
 739 principle based stress–displacement formulation for three-dimensional iso-
 740 geometric analysis in linear elasticity, Computer Methods in Applied Me-
 741 chanics and Engineering 394 (2022) 114920.

- 742 [53] H. Casquero, M. Golestanian, Vanquishing volumetric locking in quadratic
 743 NURBS-based discretizations of nearly-incompressible linear elasticity:
 744 CAS elements, *Computational Mechanics* 73 (6) (2024) 1241–1252.
- 745 [54] A. Huerta, Y. Vidal, P. Villon, Pseudo-divergence-free element free
 746 Galerkin method for incompressible fluid flow, *Computer Methods in Ap-
 747 plied Mechanics and Engineering* 193 (12-14) (2004) 1119–1136.
- 748 [55] C. T. Wu, W. Hu, J. S. Chen, A meshfree-enriched finite element method
 749 for compressible and near-incompressible elasticity, *International Journal
 750 for Numerical Methods in Engineering* 90 (7) (2012) 882–914.
- 751 [56] T. Vu-Huu, C. Le-Thanh, H. Nguyen-Xuan, M. Abdel-Wahab, A high-
 752 order mixed polygonal finite element for incompressible Stokes flow analy-
 753 sis, *Computer Methods in Applied Mechanics and Engineering* 356 (2019)
 754 175–198.
- 755 [57] E. Stein, R. de Borst, T. J. R. Hughes (Eds.), *Encyclopedia of Compu-
 756 tational Mechanics*, John Wiley, Chichester, West Sussex, 2004.
- 757 [58] I. Babuška, J. Osborn, Eigenvalue Problems, in: *Handbook of Numerical
 758 Analysis*, Vol. 2 of *Finite Element Methods (Part 1)*, Elsevier, 1991, pp.
 759 641–787.
- 760 [59] K. Yosida, *Functional Analysis*, 6th Edition, Classics in Mathematics,
 761 Springer-Verlag, Berlin Heidelberg, 1995.
- 762 [60] J. Wu, D. Wang, An accuracy analysis of Galerkin meshfree methods ac-
 763 counting for numerical integration, *Computer Methods in Applied Mechan-
 764 ics and Engineering* 375 (2021) 113631.
- 765 [61] S. Timoshenko, J. Goodier, *Theory of Elasticity*, Engineering Mechanics
 766 Series, McGraw-Hill, 1969.
- 767 [62] S. Reese, P. Wriggers, B. D. Reddy, A new locking-free brick element tech-
 768 nique for large deformation problems in elasticity, *Computers & Structures*
 769 75 (3) (2000) 291–304.
- 770 [63] S. C. Brenner, L. R. Scott, *The Mathematical Theory of Finite Element
 771 Methods*, Springer, New York, 2008.

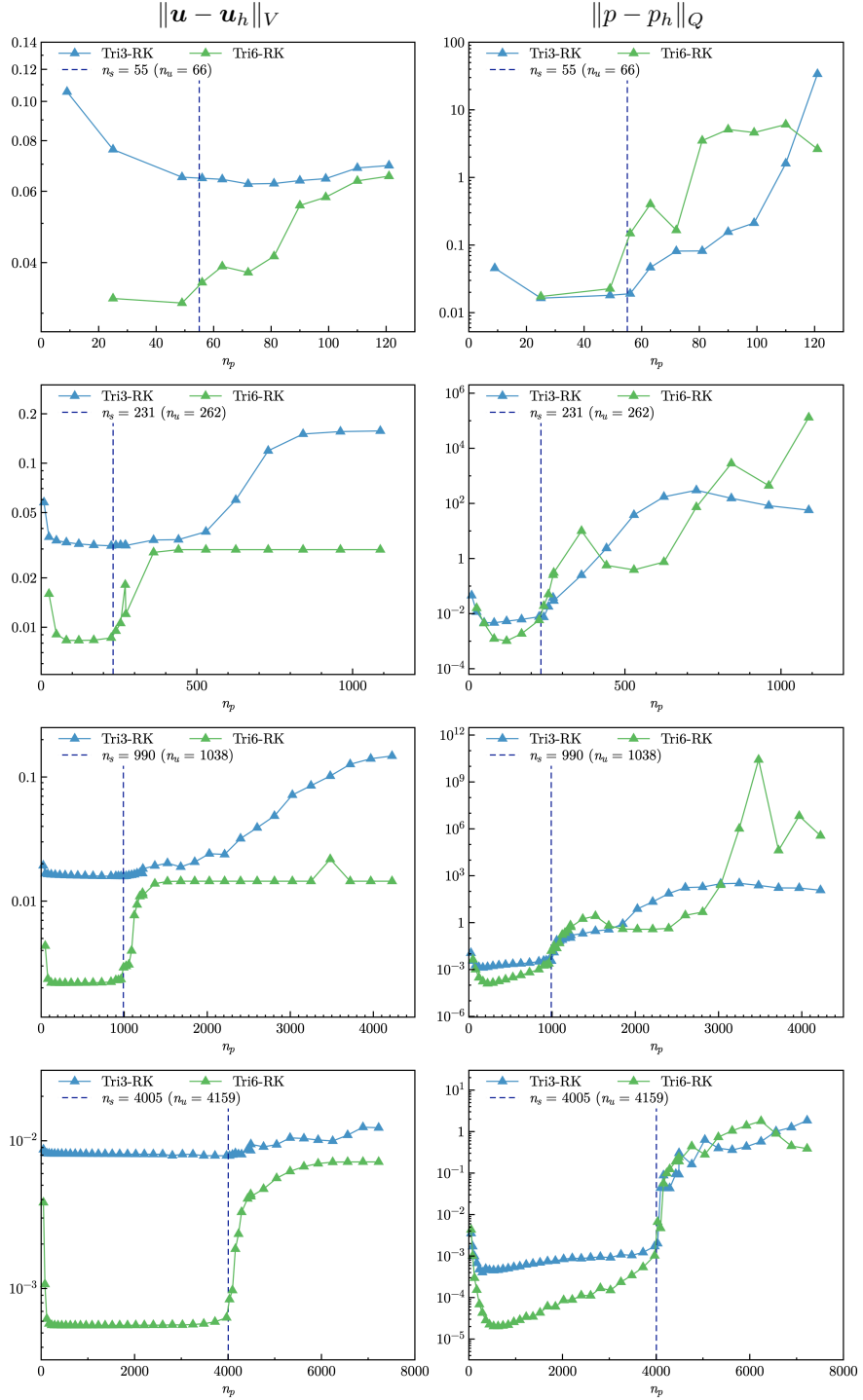


Figure 19: Strain and pressure errors vs. n_p for plate with hole problem

772 **Appendix A. Error estimator for mixed-formulation**

773 In this appendix, the traditional error estimators for mixed-formulation are
 774 illustrated herein, the proof is referred to [63]. For incompressible elasticity
 775 problems, i.e. $\kappa \rightarrow \infty$, $c(q, p) = 0$, the weak formula of Eq. (14) is rewritten as:
 776 Find $\mathbf{u}_h \in V_h, p_h \in Q_h$,

$$\begin{aligned} a(\mathbf{v}_h, \mathbf{u}_h) + b(\mathbf{v}_h, p_h) &= f(\mathbf{v}_h), & \forall \mathbf{v}_h \in V_h \\ b(\mathbf{u}_h, q_h) &= 0, & \forall q_h \in Q_h \end{aligned} \quad (\text{A.1})$$

777 According to the definition of bilinear form b in Eq. (10), for a $\mathbf{u}_h \in \ker \mathcal{P}_h$, then
 778 the second equation of Eq. (A.1) is naturally satisfied. Thus, the above weak
 779 formulation can be equivalently split into the following two steps: Firstly, find
 780 $\mathbf{u}_h \in \ker \mathcal{P}_h$,

$$a(\mathbf{v}_h, \mathbf{u}_h) = f(\mathbf{v}_h), \quad \forall \mathbf{v}_h \in \ker \mathcal{P}_h \quad (\text{A.2})$$

781 After determine \mathbf{u}_h , then find $p_h \in Q_h$,

$$b(\mathbf{v}_h, p_h) = f(\mathbf{v}_h) - a(\mathbf{v}_h, \mathbf{u}_h), \quad \forall \mathbf{v}_h \in V_h \quad (\text{A.3})$$

782 To further analyze the error of mixed-formulation, the following properties
 783 of bilinear forms a and b should be defined [63]:

784 • **Continuity:**

$$a(\mathbf{v}, \mathbf{u}) \leq C_a \|\mathbf{v}\|_V \|\mathbf{u}\|_V, \quad \forall \mathbf{v}, \mathbf{u} \in V \quad (\text{A.4})$$

$$b(\mathbf{v}, q) \leq C_b \|\mathbf{v}\|_V \|q\|_Q, \quad \forall \mathbf{v} \in V, \forall q \in Q \quad (\text{A.5})$$

785 • **Coercivity:**

$$\|\mathbf{v}\|_V \leq \frac{1}{\alpha} \sup_{\mathbf{w} \in V} \frac{|a(\mathbf{v}, \mathbf{w})|}{\|\mathbf{w}\|_V}, \quad \forall \mathbf{v} \in V \quad (\text{A.6})$$

786 • **Inf-sup condition:**

$$\|q\|_Q \leq \frac{1}{\beta} \sup_{\mathbf{v} \in V} \frac{|b(\mathbf{v}, q)|}{\|\mathbf{v}\|_V}, \quad \forall q \in Q \quad (\text{A.7})$$

787 where C_a and C_b are positive constants independent of mesh size h . α and β
 788 are the coercivity and inf-sup constants, respectively, which will influence the
 789 accuracy of mixed-formulation.

790 For the error of displacement, the Céa's Theorem used for the error analysis
 791 of traditional Galerkin formulation is not always valid for mixed-formulation.
 792 This is because most of mixed-formulation can not ensure $\ker \mathcal{P}_h \subset \ker \mathcal{P}$ to
 793 maintain the orthogonality of bilinear form a that is required in the proof of
 794 Céa's Theorem. So we first introduce the following error estimator for displacement
 795 in the case of $\ker \mathcal{P}_h \not\subset \ker \mathcal{P}$. For any $\mathbf{v}_h \in \ker \mathcal{P}_h$, considering the triangle

⁷⁹⁶ inequality, the coercivity in Eq. (A.6) and the continuity in Eq. (A.4), we have:

$$\begin{aligned}
\|\mathbf{u} - \mathbf{u}_h\|_V &\leq \|\mathbf{u} - \mathbf{v}_h\|_V + \|\mathbf{v}_h - \mathbf{u}_h\|_V \\
&\leq \|\mathbf{u} - \mathbf{v}_h\|_V + \frac{1}{\alpha} \sup_{\mathbf{w}_h \in \ker \mathcal{P}_h} \frac{|a(\mathbf{v}_h - \mathbf{u}_h, \mathbf{w}_h)|}{\|\mathbf{w}_h\|_V} \\
&\leq \|\mathbf{u} - \mathbf{v}_h\|_V + \frac{1}{\alpha} \sup_{\mathbf{w}_h \in \ker \mathcal{P}_h} \frac{|a(\mathbf{v}_h - \mathbf{u}, \mathbf{w}_h)| + |a(\mathbf{u} - \mathbf{u}_h, \mathbf{w}_h)|}{\|\mathbf{w}_h\|_V} \quad (\text{A.8}) \\
&\leq (1 + \frac{C}{\alpha}) \|\mathbf{u} - \mathbf{v}_h\|_V + \frac{1}{\alpha} \sup_{\mathbf{w}_h \in \ker \mathcal{P}_h} \frac{|a(\mathbf{u} - \mathbf{u}_h, \mathbf{w}_h)|}{\|\mathbf{w}_h\|_V}
\end{aligned}$$

⁷⁹⁷ According to Eqs. (A.2), (A.3) and continuity in Eq. (A.5), the second term on
⁷⁹⁸ the right hand side of above equation can be rewritten as:

$$\begin{aligned}
\sup_{\mathbf{w}_h \in \ker \mathcal{P}_h} \frac{|a(\mathbf{u} - \mathbf{u}_h, \mathbf{w}_h)|}{\|\mathbf{w}_h\|_V} &= \sup_{\mathbf{w}_h \in \ker \mathcal{P}_h} \frac{|a(\mathbf{u}, \mathbf{w}_h) - f(\mathbf{w}_h)|}{\|\mathbf{w}_h\|_V} \\
&= \sup_{\mathbf{w}_h \in \ker \mathcal{P}_h} \frac{|b(\mathbf{w}_h, p)|}{\|\mathbf{w}_h\|_V} \quad (\text{A.9}) \\
&= \sup_{\mathbf{w}_h \in \ker \mathcal{P}_h} \frac{|b(\mathbf{w}_h, p - q_h)|}{\|\mathbf{w}_h\|_V} \\
&\leq C_b \|p - q_h\|_Q
\end{aligned}$$

⁷⁹⁹ where q_h is an arbitrary variable in Q_h . Combining the Eqs. (A.8) and (A.9),
⁸⁰⁰ the following error estimator for displacement can be obtained:

$$\|\mathbf{u} - \mathbf{u}_h\|_V \leq (1 + \frac{C_a}{\alpha}) \inf_{\mathbf{v}_h \in \ker \mathcal{P}_h} \|\mathbf{u} - \mathbf{v}_h\|_V + \frac{C_b}{\alpha} \inf_{q_h \in Q_h} \|p - q_h\|_Q \quad (\text{A.10})$$

⁸⁰¹ Furthermore, for the error estimator of pressure, according to the first equa-
⁸⁰² tion of Eq. (6) and $V_h \subset V$, we have:

$$b(\mathbf{v}_h, p) = f(\mathbf{v}_h) - a(\mathbf{v}_h, \mathbf{u}), \quad \forall \mathbf{v}_h \in V_h \quad (\text{A.11})$$

⁸⁰³ and then subtracting Eq. (A.11) from Eq. (A.3) yields:

$$b(\mathbf{v}_h, p - p_h) = -a(\mathbf{v}_h, \mathbf{u} - \mathbf{u}_h), \quad \forall \mathbf{v}_h \in V_h \quad (\text{A.12})$$

⁸⁰⁴ In this context, for any $q_h \in Q_h$, invoking the triangle inequality, Eqs. (A.7)
⁸⁰⁵ and (A.5) leads to:

$$\begin{aligned}
\|p - p_h\|_Q &\leq \|p - q_h\|_Q + \|q_h - p_h\|_Q \\
&\leq \|p - q_h\|_Q + \frac{1}{\beta} \sup_{\mathbf{v} \in V_h} \frac{|b(\mathbf{v}_h, q_h - p_h)|}{\|\mathbf{v}_h\|_V} \\
&\leq \|p - q_h\|_Q + \frac{1}{\beta} \sup_{\mathbf{v} \in V_h} \frac{|a(\mathbf{v}_h, \mathbf{u} - \mathbf{u}_h)| + |b(\mathbf{v}_h, p - q_h)|}{\|\mathbf{v}_h\|_V} \quad (\text{A.13}) \\
&\leq \frac{C_a}{\beta} \|\mathbf{u} - \mathbf{u}_h\|_V + (1 + \frac{C_b}{\beta}) \|p - q_h\|_Q
\end{aligned}$$

806 Consequently, the error estimator for pressure can be given by:

$$\|p - p_h\|_Q \leq \frac{C_a}{\beta} \|\mathbf{u} - \mathbf{u}_h\|_V + \left(1 + \frac{C_b}{\beta}\right) \inf_{q_h \in Q_h} \|p - q_h\|_Q \quad (\text{A.14})$$

807 Obviously, the error estimators of Eqs. (A.10) and (A.14) are both related
 808 to the coercivity constant α , inf-sup constant β and the approximability of
 809 spaces $\ker \mathcal{P}_h$, Q_h , in which the approximability is usually measured by the
 810 interpolation error of approximation method. However, the approximability
 811 of space $\ker \mathcal{P}_h$ is not trivial to be evaluated directly. To further evaluate the
 812 approximability of space $\ker \mathcal{P}_h$, let a variable $\mathbf{w}_h \in V_h \setminus \ker \mathcal{P}_h$ to satisfy the
 813 following relationship:

$$\inf_{\bar{\mathbf{v}}_h \in \ker \mathcal{P}_h} \|\mathbf{u} - (\bar{\mathbf{v}}_h + \mathbf{w}_h)\|_V = \inf_{\mathbf{v}_h \in V_h} \|\mathbf{u} - \mathbf{v}_h\|_V \quad (\text{A.15})$$

814 such that the approximability of space $\ker \mathcal{P}_h$ can be transformed to that of
 815 space V_h that is easy to be measured. If $\mathbf{w}_h = \mathbf{0}$, $\ker \mathcal{P}_h$ has the identical
 816 approximability with V_h :

$$\inf_{\bar{\mathbf{v}}_h \in \ker \mathcal{P}_h} \|\mathbf{u} - \bar{\mathbf{v}}_h\|_V = \inf_{\mathbf{v}_h \in V_h} \|\mathbf{u} - \mathbf{v}_h\|_V \quad (\text{A.16})$$

817 If $\mathbf{w}_h \neq \mathbf{0}$, leading a triangle inequality we have:

$$\|\mathbf{u} - \bar{\mathbf{v}}_h\|_V \leq \|\mathbf{u} - (\bar{\mathbf{v}}_h + \mathbf{w}_h)\|_V + \|\mathbf{w}_h\|_V \quad (\text{A.17})$$

818 where, reconsidering the Eq. (26) in Lemma 1, as $\mathbf{w}_h \in V_h \setminus \ker \mathcal{P}_h$ and $\mathbf{w}_h \neq \mathbf{0}$,
 819 the following relation can be obtained:

$$\|\mathbf{w}_h\|_V \leq \frac{1}{\beta} \|\mathcal{P}_h \mathbf{w}_h\|_Q \quad (\text{A.18})$$

820 where, using Eqs. (25), (17) and considering $\mathbf{u} \in \ker \mathcal{P}$, $\bar{\mathbf{v}}_h \in \ker \mathcal{P}_h$, the right
 821 hand side of above equation can further be transformed as follows:

$$\begin{aligned} \|\mathcal{P}_h \mathbf{w}_h\|_Q &= \sup_{q_h \in Q_h} \frac{|\frac{1}{\kappa}(\mathcal{P}_h \mathbf{w}_h, q_h)|}{\|q_h\|_Q} = \sup_{q_h \in Q_h} \frac{|b(\mathbf{w}_h, q_h)|}{\|q_h\|_Q} \\ &= \sup_{q_h \in Q_h} \frac{|b(\mathbf{u} - (\mathbf{w}_h + \bar{\mathbf{v}}_h), q_h)|}{\|q_h\|_Q} \quad (\text{A.19}) \\ &\leq C_b \|\mathbf{u} - (\mathbf{w}_h + \bar{\mathbf{v}}_h)\|_V \end{aligned}$$

822 With the combination of Eqs. (A.17), (A.18) and (A.19), the approximability
 823 of $\ker \mathcal{P}_h$ for the case of $\mathbf{w}_h \neq \mathbf{0}$ is given by:

$$\inf_{\bar{\mathbf{v}}_h \in \ker \mathcal{P}_h} \|\mathbf{u} - \bar{\mathbf{v}}_h\|_V \leq \left(1 + \frac{C_b}{\beta}\right) \inf_{\mathbf{v}_h \in V_h} \|\mathbf{u} - \mathbf{v}_h\|_V \quad (\text{A.20})$$